NASA TECHNICAL NOTE

NASA TN D-614

C.1

NASA TN D-614

THE TIROS LOW RESOLUTION RADIOMETER

by Frank Bartko, Virgil Kunde, Clarence Catoe,
and Musa Halev

Goddard Space Flight Center
Greenbelt, Md.

NATIONAL AERONAUTICS AND SPACE ADMINISTRATION • WASHINGTON, D. C. • SEPTEMBER 1964

THE TIROS LOW RESOLUTION RADIOMETER

By Frank Bartko, Virgil Kunde,
Clarence Catoe, and Musa Halev

Goddard Space Flight Center
Greenbelt, Md.

NATIONAL AERONAUTICS AND SPACE ADMINISTRATION

For sale by the Office of Technical Services, Department of Commerce,
Washington, D.C. 20230 -- Price $1.00

THE TIROS LOW RESOLUTION RADIOMETER

by
Frank Bartko, Virgil Kunde,
Clarence Catoe, and Musa Halev
Goddard Space Flight Center

SUMMARY

The Tiros II, III, and IV (1960 π1, 1961 ρ1 and 1962 β1) meteorological satellite experiments included a low resolution infrared radiometer of broad spectral and spatial response designed to measure the planetary heat budget of the earth. The radiometer consisted of two thermistor detectors, each mounted at the base of a reflective cone. One detector was coated black and was sensitive to reflected solar and long wave terrestrial radiation. The second detector was coated white and was sensitive primarily to the long wave terrestrial radiation. Simultaneous evaluation of the energy balance equation for each detector yields the earth's apparent blackbody temperature and albedo.

The first portion of this paper presents the physical and optical characteristics of the radiometer, the calibration, and the procedure for determining the coefficients of the energy balance equations from the calibration data. The second portion of the paper discusses the procedure for reducing the data and presents an error analysis of the radiation data from a Tiros III orbit. Efforts to improve the performance of the low resolution radiometer and a summary of the status of the low resolution radiometer program are also presented.

CONTENTS

Summary i

List of Symbols v

INTRODUCTION. 1

DESCRIPTION OF THE RADIOMETER 3

CALIBRATION MEASUREMENTS 6

- Thermal Calibration. 7
- Reflected Solar Radiation Calibration 10
- Time Constant Measurements 13
- Calibration of the Radiometer Components 13
- Subcarrier Oscillator Calibration. 14
- Additional Measurements 15
- Sources of Error. 19
- Reduction of the Calibration Data 20

DETERMINATION OF THE COEFFICIENTS OF THE HEAT TRANSFER EQUATION 20

- Thermal Coefficients 21
- Reflected Solar Radiation Coefficient 23

DATA PROCESSING AND REDUCTION 24

DATA COVERAGE LIMITATIONS. 31

POST-LAUNCH OBSERVATIONS 32

SUMMARY OF THE TIROS LOW RESOLUTION RADIOMETER PROGRAM 32

IMPROVEMENT EFFORTS 33

CONCLUSION 33

ACKNOWLEDGMENTS 34

References 34

LIST OF SYMBOLS

A	Albedo of the earth, defined as the reflectance of the area on the earth viewed by the radiometer, averaged spatially over the solid angle defined by the field of view, and averaged spectrally over the solar spectrum
B	Elevation angle of the sun
B'	Angle between the incoming light beam and the plane of diffuse paper
C	Thermopile constant for diffuse radiation
C_1	Thermopile constant for beam radiation
f	Frequency of the oscillator
H_s	Solar radiation incident upon the white paper of the calibration apparatus after being modified by the earth's atmosphere and a reflecting mirror
K	Thermal conductive coefficient, watts/°K-cm^2
K_1	Thermal coefficient of proportionality
K_2	Thermal coefficient of proportionality
K_3	Reflected solar radiation coefficient
k_1	Thermal coefficient of proportionality, equal to K_1/ϵ_t
k_2	Thermal coefficient of proportionality, equal to K_2/ϵ_t
k_2'	Thermal coefficient of proportionality, equal to $K/\sigma\epsilon_t$
k_3	Reflected solar radiation coefficient (°K^4-cm^2/watt), equal to $K_3/\sigma\epsilon_t$
P	Pressure
$R_c(\lambda)$	Spectral reflectance of a reflecting cone
R_h	Housing thermistor network resistance
R_N	Network resistance
R_{N_b}	Network resistance for the black detector
R_{N_w}	Network resistance for the white detector
R_o	Resistance of constant value
R_{o_b}	Resistance of constant value for the black detector network
R_{o_h}	Resistance of constant value for the housing thermistor network
R_{o_w}	Resistance of constant value for the white detector network
$R_p(\lambda)$	Spectral reflectance of a paint coating on the thermistor detector
R_t	Thermistor detector resistance
R_{t_b}	Black detector resistance
R_{t_w}	White detector resistance

R_1	Reference resistance, near the upper limit of the bandwidth
R_3	Reference resistance, near the lower limit of the bandwidth
r_p	Spectral reflectance of diffuse paper
S	Solar constant
S_i	Sensistor resistance
S_j	Sensistor resistance
S_1	Sensistor resistance for the detector leg of the black detector network
S_2	Sensistor resistance for the fixed resistance leg of the black detector network
S_3	Sensistor resistance for the fixed resistance leg of the white detector network
S_4	Sensistor resistance for the detector leg of the white detector network
T_b	Black thermistor detector equilibrium temperature
T_c	Housing temperature of the medium resolution radiometer
T_E	Oscillator temperature
T_e	Apparent earth blackbody temperature, corresponding to the thermal emission received from the earth's surface and intervening atmosphere, averaged spatially over the solid angle defined by the field of view and averaged spectrally over the thermal spectrum
T_q	Quartz window temperature
T_s	Radiometer housing temperature
T_t	Thermistor detector equilibrium temperature
T_w	White thermistor detector equilibrium temperature
t	Transmittance of the quartz window
V_{bb}	Thermocouple voltage representing the blackbody cavity temperature
V_1	Thermopile response due to H_S
V_2	Thermopile response due to W_{sp}
V_3	Thermopile response due to W_{bp}
W	Total radiant emittance from the earth
W_{bp}	Radiant emittance of the diffuse paper due to tungsten bulb irradiance
W_{sp}	Radiant emittance of the diffuse paper due to solar irradiance
$\alpha_t(\lambda)$	Spectral absorptance of the painted thermistor detector
ϵ_t	Spectral emissivity of the detector
σ	Stefan-Boltzmann constant
$\phi(\lambda)$	Spectral response of the radiometer
$\phi'(\lambda)$	Auxiliary spectral response function, equal to $r_p\,\phi(\lambda)$.

THE TIROS LOW RESOLUTION RADIOMETER

by
Frank Bartko, Virgil Kunde,
Clarence Catoe, and Musa Halev
Goddard Space Flight Center

INTRODUCTION

The Tiros II, III, and IV (1960 π1, 1961 ρ1, and 1962 β1) meteorological satellites each contain two television cameras, a medium resolution scanning radiometer, a low resolution nonscanning radiometer, and a University of Wisconsin heat balance experiment. The resolution description (medium or low) refers to both the spectral and spatial optical characteristics of the radiometers. The television cameras and medium resolution radiometer have been described elsewhere (References 1-4). This paper is concerned only with the low resolution nonscanning radiometer. The mean orbital characteristics for the Tiros satellites with an operational low resolution radiometer on-board are listed in Table 1.

The low resolution radiometer was designed to measure thermal and reflected solar radiation emanating from the earth. From these two quantities, the apparent blackbody temperature and the albedo of the earth can be determined. A study of these data over an extended period of time shows, in principle, how the incoming solar energy is utilized by the earth. Such quantitative measurements could hopefully provide a firm foundation for a better study of the earth's overall energy budget. The basic principles of the experiment have been described by Hanel (Reference 5). The radiometer characteristics, the calibration procedures, and the reduction of calibration and orbital radiation data are presented here. The limitations of the radiometer and efforts to remove these limitations are also discussed.

Table 1

Tiros Mean Orbital Characteristics.

Satellite	Launch Date	Perigee Altitude (km)	Apogee Altitude (km)	Anomalistic Period (min)	Orbital Inclination (degrees)
Tiros II	11/23/60	620.6	731.3	98.27	48.53
Tiros III	7/12/61	740.5	815.6	100.41	47.90
Tiros IV	2/8/62	710.3	844.7	100.40	48.30

The physical basis of the experiment is provided by the consideration of the steady state energy gains and losses experienced by a thermistor detector exposed to the earth from a satellite about 765 km above the surface. The low resolution radiometer consists of two such thermistor detectors housed in the Tiros satellite structure. In the vacuum environment, the steady state thermal balance of each detector is given by Hanel (Reference 5) as

$$\epsilon_t \sigma T_t^4 = K_1 \sigma T_e^4 + K_2 \sigma T_s^4 + K(T_s - T_t) + K_3 S A \sin B , \tag{1}$$

where the left side is the radiative energy loss of the thermistor detector at an equilibrium temperature T_t and emissivity ϵ_t. The first and second terms on the right represent the radiative coupling of the detector with the earth at an apparent blackbody temperature T_e and the radiometer housing at a temperature T_s, respectively. The third term on the right represents the conductive coupling with the satellite structure, and the fourth term is the earth's reflected solar radiation, where S is the solar constant, A is the albedo, as defined below, and B is the solar elevation angle at the center of the viewed area. It is necessary to include the coupling of the detectors with the satellite since it is impossible to thermally isolate the detectors completely from the satellite structure. The thermal coefficients of proportionality, K_1, K_2, and K, and the proportionality coefficient for reflected solar radiation, K_3, include the geometrical and optical characteristics of the detectors.

Dividing Equation 1 by $\epsilon_t \sigma$ yields the convenient form

$$T_t^4 = k_1 T_e^4 + k_2 T_s^4 + k_2' (T_s - T_t) + k_3 S A \sin B \tag{2}$$

In Equation 2 the albedo is the reflectance of the area on the earth viewed by the radiometer, averaged spatially over the solid angle defined by the field of view and averaged spectrally over the solar spectrum. The apparent earth temperature is the blackbody temperature corresponding to the thermal emission received from the earth's surface and intervening atmosphere, averaged spatially in the same manner as for the albedo and averaged spectrally over the thermal spectrum. When the boundary conditions $S = 0$ and $T_t = T_e = T_s$ are applied, then $k_1 + k_2 = 1.0$.

If the T_t's and T_s's are measured and the k's are determined by calibration, the solution of two such equations for two detectors of sufficiently different optical characteristics will yield the desired values of T_e and A. The instrument considered here was designed to provide for each detector values of approximately 0.9 for k_1 and about 0.1 for k_2.

The low resolution radiometer is mounted on the baseplate of the Tiros satellite so that it views the earth along the direction of the satellite spin axis. The location of the radiometer can be seen in Figure 1. The spin-stabilized satellite is space oriented so that the radiometer has its field of view filled by the earth for a maximum time of 1/5 of the orbital period. The geometry of the viewing area at different parts of the orbit is shown in Figure 2. The orientation and shielding provided by the satellite are such that the detectors should never receive direct solar radiation.

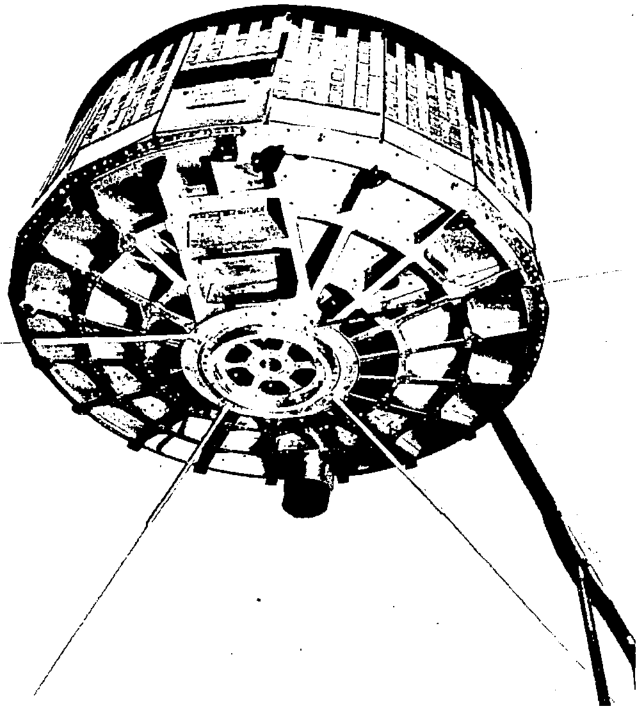

Figure 1—Tiros meteorological satellite. A wide angle television lens protrudes from the baseplate and the round aperture near the top of the photograph is the location of the low resolution radiometer.

DESCRIPTION OF THE RADIOMETER

The radiometer structure is illustrated in Figure 3 which shows a front view of the instrument (Reference 4). Two highly aluminized truncated Mylar cones are mounted on a 3 in. diameter, gold-plated, aluminum plate. At the base of each cone is mounted a thermistor detector fastened to the mylar base by a grid of fibers of low thermal conductivity. The fiber strength has proved to be more than sufficient as evidenced by numerous successful vibration tests on the radiometer. The two thermistors comprise the heart of the instrument. The resistance of these detectors is a function of the energy flux which they absorb. The response is the value of the resistance of the detector, which is further processed by additional electronics and transmitted to the earth. Further

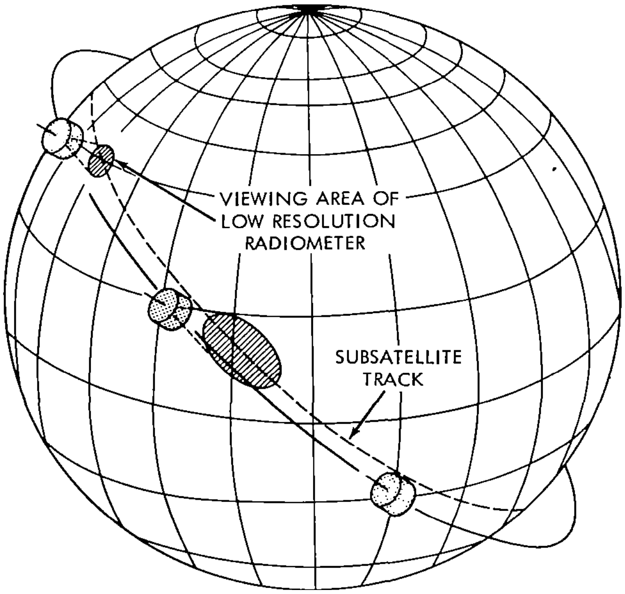

Figure 2—Examples of the viewing area of the low resolution radiometer.

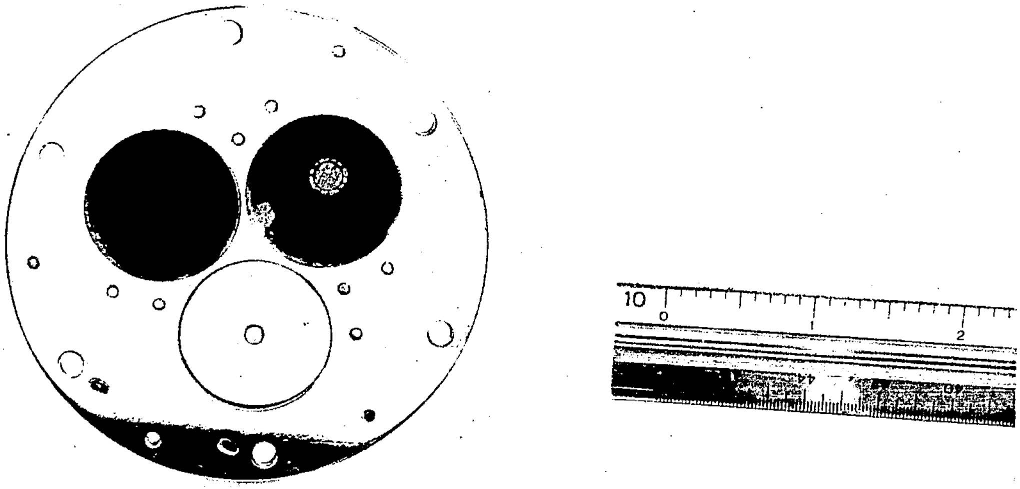

Figure 3—The low resolution radiometer. The white thermistor detector can be seen at the base of the aluminized cone on the right. The black thermistor detector is located in the cavity on the left.

details will be described below. Each of the two platinum electrical leads attached to each detector winds about one of the mounting grid fibers and passes through the base of the cone wall to a network of three additional resistances. Since the response is the value of the detector resistance, three additional resistances are provided to compensate for effects due to housing temperature changes on the detector. The network is illustrated by Figure 4. R_N is the resultant resistance of the four element network consisting of resistances of the thermistor detector (R_t), two sensistors (S_i, S_j), and a fixed resistance (R_o).

The resistance values and their temperature coefficients are chosen to give the best compensation for housing temperature effects on the detector. The wire-wound resistance R_o is given a fixed value which is independent of temperature. The response of each detector is actually found by calibrating R_N as a function of housing temperature and target temperature and then calculating R_t from R_N. The following relationship holds between the various elements of the resistance network:

$$R_t = \frac{R_N\left(R_o + S_j\right) - S_i\left(R_o + S_j - R_N\right)}{R_o + S_j - R_N} . \qquad (3)$$

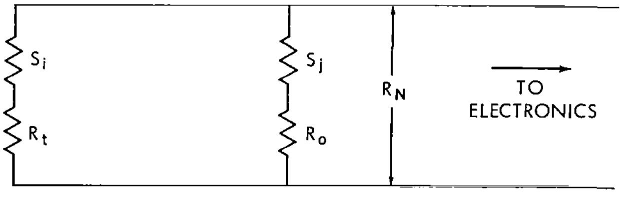

Figure 4—Schematic of the resistance network for the thermistor detector of the low resolution radiometer. R_N is the resultant resistance of the four-element network consisting of resistances of the thermistor detector R_t, two sensistors S_i and S_j, and a fixed resistance R_o.

The radiometer housing temperature is determined from the resistance R_h of a network consisting of a thermistor and a fixed resistor connected in parallel. A back cover plate is provided to protect the delicate construction of the cones and the electrical components. The surfaces of the cover plate are highly polished to minimize radiation coupling with the satellite. The total weight of the instrument is 46.3 gm. A schematic of the radiometer is shown in Figure 5.

The most important optical characteristics of the radiometer are its spectral sensitivity, field of view, and response time. It was attempted to tailor each of these quantities to the desired objectives of the experiment and to make them compatible with the Tiros satellite.

The spectral characteristics of the radiometer were determined by coatings of paint applied to each detector. These characteristics were based on the following considerations. The total radiant emittance, W, emanating from the earth consists of two spectral components, expressed quantitatively by

$$W = W_{\text{earth emission } (\lambda > 4\mu)} + W_{\text{reflected solar radiation } (\lambda < 4\mu)} .$$

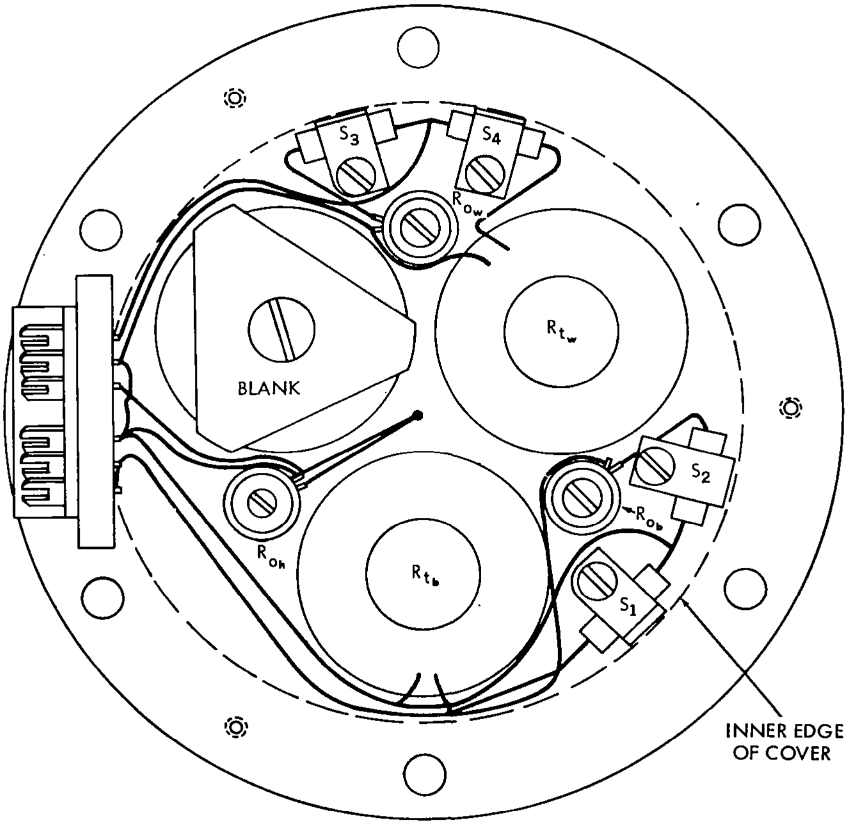

Figure 5—Schematic of the low resolution radiometer. R_{t_b}, S_1, S_2 and R_{o_b} comprise the network resistances for the black cone and R_{t_w}, S_3, S_4, and R_{o_w} comprise the network resistances for the white cone. The housing temperature T_s is determined from the resistance R_h of a separate thermistor and an associated fixed resistance R_{o_h}.

The values of these components can be obtained by measuring each separately or measuring the total and one of the components. In the present case the total energy and the terrestrial emission were selected for measurement. One thermistor was coated with a black paint designed to absorb, as uniformly and completely as possible, radiation over all wavelengths of the spectrum. The second thermistor was painted white in order to absorb primarily the terrestrial emission and be spectrally blind to the reflected solar radiation from the earth. The differences in temperatures of these thermistors then provide a means for calculating the values of T_e and A.

The field-of-view characteristics of each detector are determined by the angular aperture of the cone and the ratio of cone length to detector radius. The half-angle of the cones is about 27 degrees and was chosen to: (1) optimize the radiation exchange of the detectors with the earth's surface, (2) provide integrated values for quantities that are averaged over large areas, and (3) view an area on the earth comparable in size with that viewed by the television cameras. At the altitude of the Tiros satellites ($\approx$765 km), when the satellite spin axis is coincident with the local vertical of the earth, circular areas of approximately 870 and 1050 km in diameter are viewed by the radiometer and wide-angle television camera, respectively.

The time response of each detector is directly proportional to its thickness. This includes the thickness of the actual detector and that of the paint. The value chosen for the time constant had to be compatible with the radiometer field of view and the orbital velocity of Tiros. The design figure for the radiometer was about 30 sec and measurements indicate a value of about 35 sec.

CALIBRATION MEASUREMENTS

The values of the thermal and reflected solar radiation coefficients of the heat transfer equation must be known as accurately as possible. Since these coefficients involve the geometric and optical parameters of the radiometer in a complex fashion, an empirical method is the best means for obtaining their values.

While the radiometer is viewing the earth, the energy flux incident upon the radiometer consists of the thermal emission from the earth and its atmosphere (4 to 40μ) and the reflected solar radiation (0.2 to 4μ). It is quite difficult to simulate these components in a realistic fashion with a single standard calibration source. As a result, the calibration was separated into two parts, each of which could be handled by separate standard calibration sources. In each part, the calibration consisted of placing the radiometer in a small vacuum chamber and exposing each detector to a target of known and variable radiant emittance. A vacuum environment is necessary since the heat balance of the detectors had to be controlled by radiative processes during calibration just as it is in the vacuum environment in orbit. If air were present about the detector, the conduction of heat to and from the detector by the air would overshadow the heat transfer by radiation. Vacuum chamber pressures of 10^{-5} mm Hg were used for the calibration of the instrument. The housing temperature of the radiometer became a parameter and was varied through the expected temperature range for each value of target radiant emittance for the thermal radiation calibration. The reflected solar radiation calibration was performed at one single housing temperature only, since corrections for the entire range of housing temperatures had already been determined in the thermal calibration.

Thermal Calibration

The first portion of the calibration was designed to simulate the expected thermal emission from the earth. The radiometer was exposed to a blackbody cavity of known temperature. The whole apparatus was placed in a vacuum chamber as illustrated in Figures 6 and 7. The radiometer was mounted in good thermal contact to a metal plate with cutouts in the center which permit

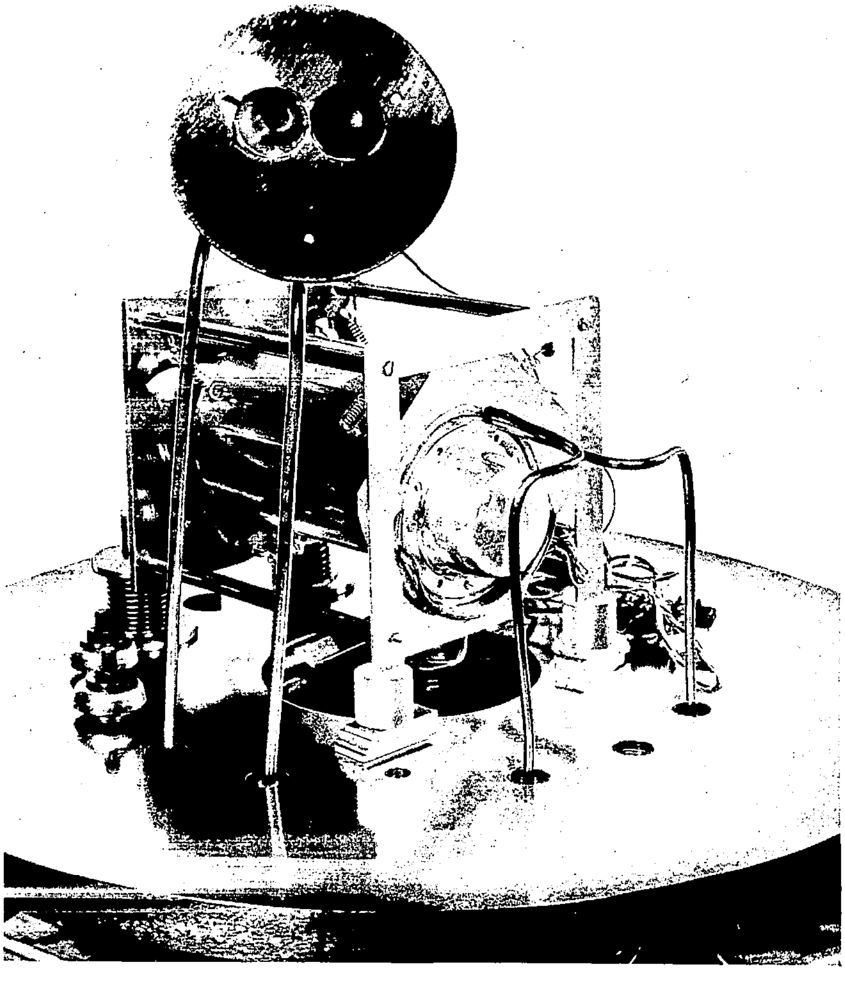

Figure 6—The laboratory calibration apparatus. A low resolution radiometer is positioned in front of the blackbody cavity. The upper part of the photograph shows a second radiometer in position for the reflected solar radiation calibration.

Figure 7—The calibration stand and vacuum chamber. The radiometer mounted for the reflected solar radiation calibration can be seen through the quartz window of the vacuum chamber.

each detector to view the cavity directly. The temperature of the metal plate and radiometer could be varied by circulating liquids of various temperatures through a tubing soldered onto the plate. The housing temperature range was varied from -20°C to +60°C, by using alcohol cooled with various amounts of dry ice for the cold temperatures and heated by an electrical heater for the high temperatures. The blackbody temperature, -100°C to +60°C, was likewise controlled by circulating liquids; it was measured by a sensitive voltmeter with the use of a calibrated thermocouple placed inside the cavity. Liquid nitrogen for the lowest temperatures, alcohol with varying amounts of dry ice, and electrical heaters were used to vary the cavity temperature.

The procedure, then, consisted of holding the temperature of the blackbody cavity constant and varying the temperature of the housing. The measurements were then repeated for each detector with a different value of the blackbody temperature, until the complete range was covered. A set of calibration curves was then developed showing the response for each detector as a function of the housing temperature with the cavity temperature as a parameter. Curves are shown in Figure 8 for a typical white detector.

Figure 9 illustrates the procedure for the thermal radiation calibration measurements. The calibration was designed to simulate the actual electrical environment existing in Tiros. Each detector can be connected through a switching box to a subcarrier oscillator. The network resistance of the detector then controls the output frequency of the oscillator within the frequency band 425 - 475 cps. The frequency output of the oscillator passes to a frequency counter and is recorded by a digital printer. The response of the frequency-controlled subcarrier oscillator was calibrated at the same time. Therefore, immediately after the measurement, a decade box was connected to the input of the oscillator and the resistance R_N which corresponds to the measured frequency was found.

Figure 10 illustrates the calibration curve for the housing thermistor network resistance. This calibration can be made in terms of R_h,

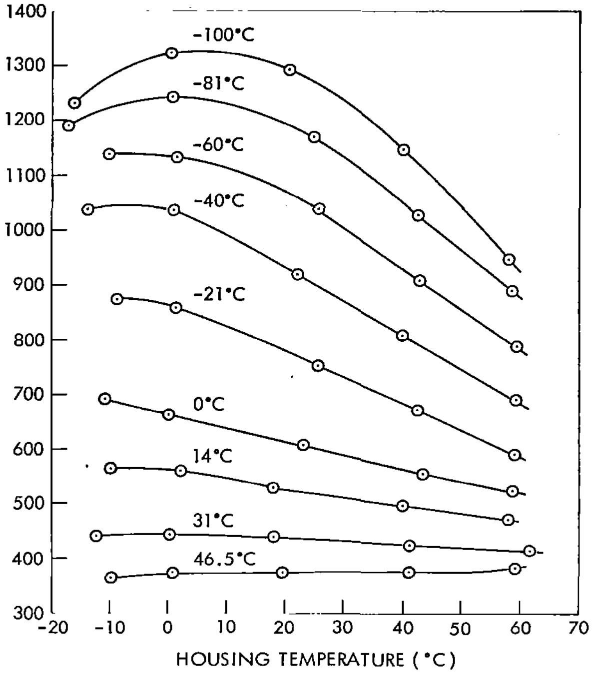

Figure 8—Thermal test data for a white detector. The parameter for the curves is the apparent earth blackbody temperature.

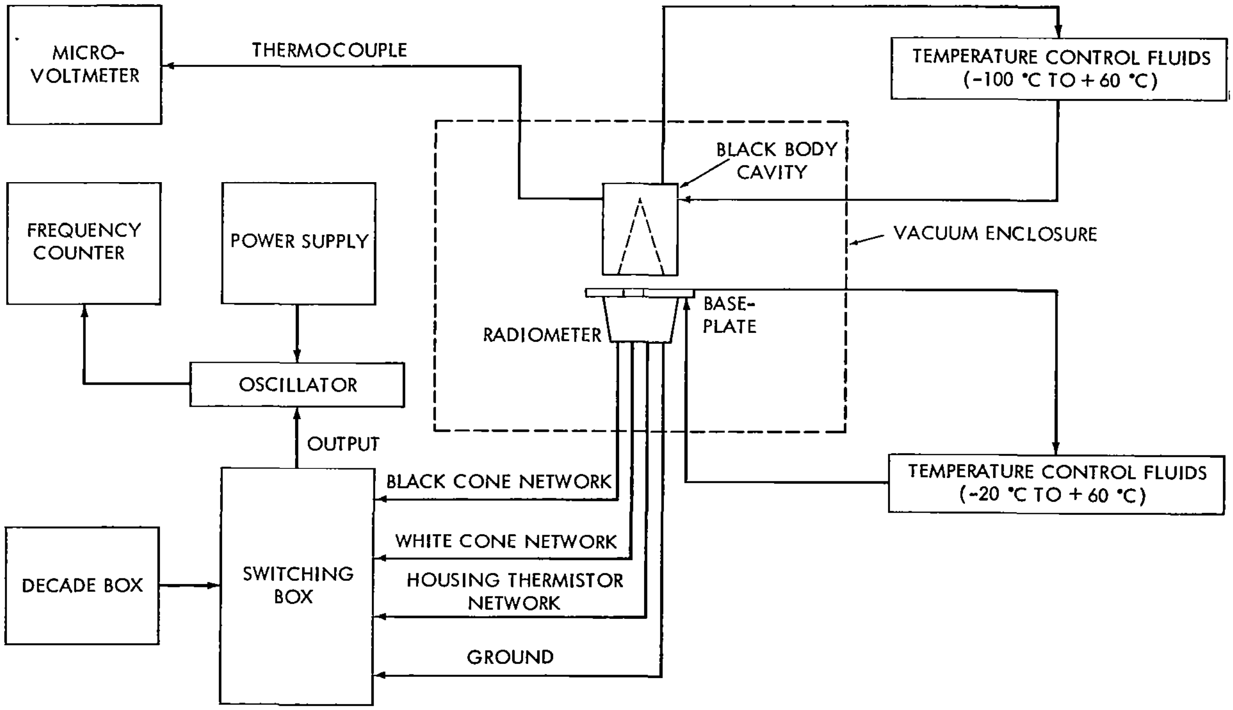

Figure 9—Schematic diagram of the thermal radiation calibration setup.

rather than of the thermistor resistance itself, because there are no temperature effects on the fixed resistor.

The unreduced thermal calibration data consisted of R_h, V_{bb}, R_{N_b}, and R_{N_w}, where the subscripts b and w represent the black and white detectors. These must be converted to their respective detector equilibrium temperatures. The first two conversions are accomplished readily, but the last two require more extensive reduction. The value of R_h is taken directly from a thermistor housing temperature curve as is shown in Figure 10. The value V_{bb} is converted by a calibration chart for the thermocouple. The reduction of the detector network resistances is discussed later.

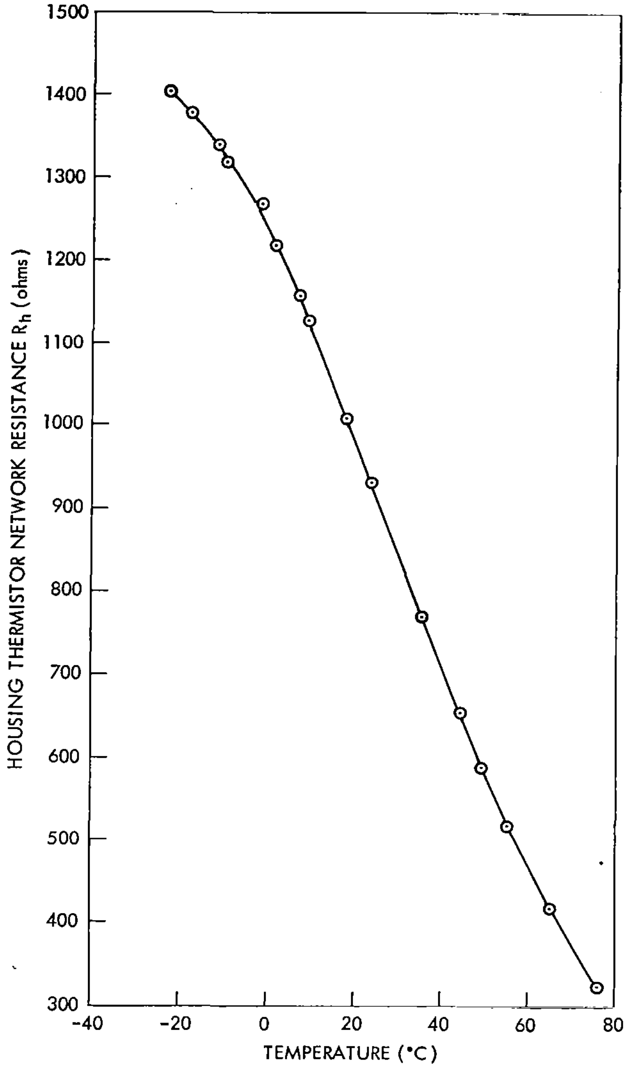

Figure 10—Radiometer housing thermistor network response as a function of temperature.

Reflected Solar Radiation Calibration

The second portion of the calibration involved an attempt to simulate the reflected solar radiation from the earth. The calibration consisted of exposing each detector to a diffuse light source of known and variable radiant emittance. As before, the radiometer was placed in the vacuum chamber, but in a position to view a large sheet of white diffuse paper through a quartz window. The illuminated paper was placed in a position such that it filled the fields of view of both detectors. The source of radiation used to illuminate the white diffuse paper consisted of an array of eight blue-dyed tungsten bulbs. The tungsten bulbs were used for two reasons: (1) A greater variation in radiant emittance could be attained by the use of an array of bulbs as contrasted with a single value obtained by using the sun directly at any given time, and (2) for practical calibration purposes, an artificial source was necessary to avoid delay caused by unpredictable weather conditions. A great disadvantage occurs however since the spectral energy distribution is different from that of the sun. These bulbs were used to simulate solar radiation under the assumption of a flat spectral response for the radiometer over the spectral range of the solar radiation and the bulbs, so that the radiometer response depended only on the total energy incident on it. (The validity of this assumption is discussed later when the spectral response measurements are presented.) Hence, the network resistances of the black and white detectors were calibrated against the total energy output of the bulbs, expressed in terms of the solar constant by using an Eppley thermopile as the standard of measurement. First, however, the thermopile had to be calibrated in terms of the existing experimental conditions. This was necessary because of differences in the types of sources viewed in the original calibration of the thermopile and in the radiometer calibration. The original thermopile calibration refers to beam radiation whereas the radiometer calibration uses diffuse radiation. Because of these differences, the original calibration data for the thermopile, supplied by the manufacturer, could not be used directly to convert its output voltage to total energy received and it was necessary to calibrate the thermopile for radiation from the same diffuse target as seen by the radiometer. The experimental arrangement is illustrated schematically in Figure 11. A 30 in. diameter aluminized, optically flat mirror directed a beam of sunlight onto a sheet of diffuse white paper. By assuming that the paper obeys Lambert's Law, measurement of the angle (B') between the incoming beam of solar radiation and the plane of the paper, combined with a knowledge of the solar irradiance as modified by the mirror reflectance H_s and the spectral reflectance of the diffuse paper r_p, permitted the radiant emittance of the paper W_{sp} to be calculated.

The thermopile was first placed to view the incoming solar beam. This gave a measure of H_s at the time of the measurement. The thermopile response V_1 was converted to H_s by

$$V_1 = C_1 H_s , \qquad (4)$$

where C_1 is known from the original calibration data. The thermopile was next placed to view the illuminated paper in the same fashion as the radiometer, and its response V_2 was recorded:

$$V_2 = C W_{sp} , \qquad (5)$$

where C is the constant to be determined. Since the paper was assumed to obey Lambert's Law,

$$W_{sp} = H_s \sin B' \bar{r}_p , \qquad (6)$$

where $\bar{r}_p$ is the average reflectance (over the solar spectrum) of the white diffuse paper. Substituting Equation 6 into Equation 5 gives

$$V_2 = C(H_s \sin B' \bar{r}_p) . \qquad (7)$$

Hence, by knowing V_2, B', and $\bar{r}_p$, and measuring H_s with Equation 4, the value of C can be found.

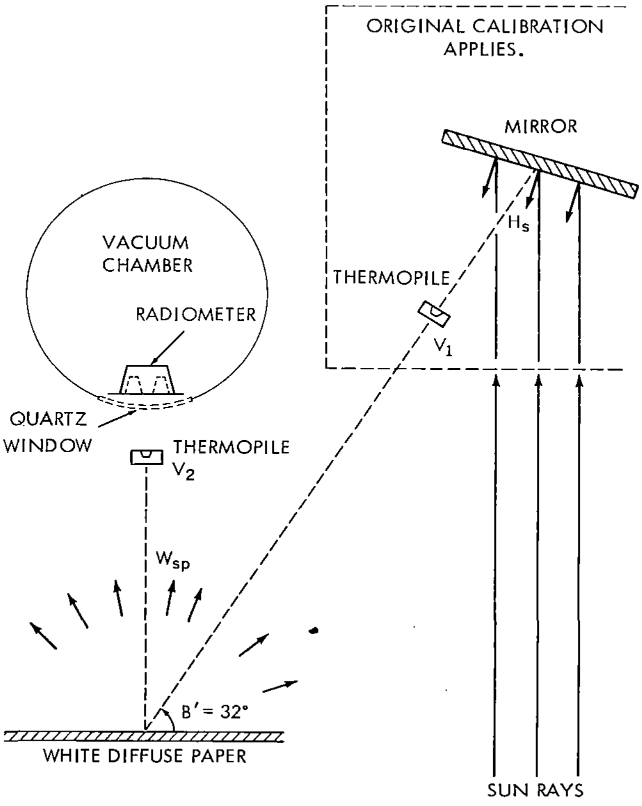

Figure 11—Two-dimensional schematic of the calibration of the thermopile for diffuse radiation in terms of reflected solar radiation.

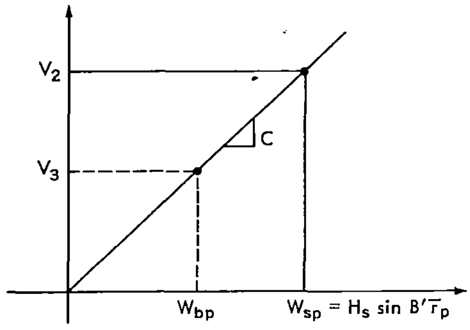

Figure 12—Graphical relationship between the thermopile response and diffuse radiation.

With C known, Equation 5 defines the calibration of the thermopile for diffuse radiation. Since the thermopile response is assumed to be spectrally flat, Equation 5 is assumed to be linear, as shown in Figure 12.

The array of eight tungsten bulbs was then placed to illuminate the white diffuse paper as shown in Figure 13. The thermopile was again placed to view the diffuse source in the same fashion as the radiometer, and its response was

$$V_3 = C W_{bp} , \tag{8}$$

where W_{bp} is the radiant emittance of the diffuse paper due to the irradiance from the tungsten bulbs. In Equation 2, the heat transfer equation, the term $S A \sin B$ may be represented by W_{bp}. A correction must be made for the transmittance (t) of the quartz window. With this correction

$$S A \sin B = V_3 \frac{t}{C} \tag{9}$$

By varying the number of tungsten bulbs used, the radiant emittance W_{bp} can be varied. The calibration of the radiometer proceeds in the following manner:

1. The radiometer housing temperature, black and white detector responses, and the quartz window temperature (T_q) are recorded prior to exposure to the tungsten bulb array.

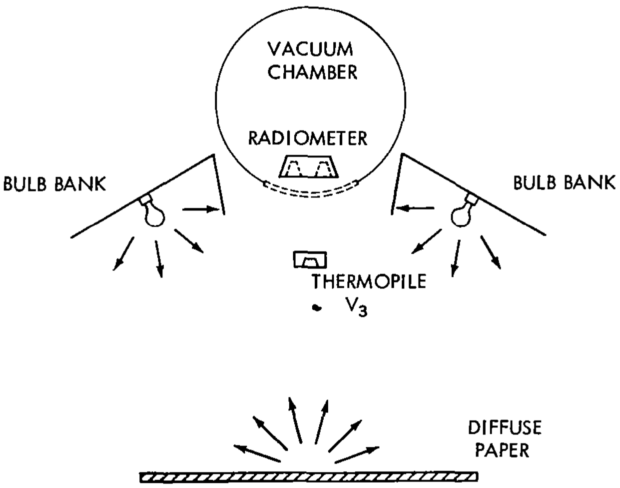

Figure 13—Schematic of the reflected solar radiation calibration of the low resolution radiometer.

2. The bulbs are turned on until an equilibrium response is attained for each detector and the above measurements are repeated. In addition, the thermopile output V_3 is recorded.

3. The measurements of steps 1 and 2 are repeated with an increasing number of bulbs in the array.

The unreduced calibration results consist of R_{N_b}, R_{N_w}, R_h, T_q, and V_3. These parameters must be converted to temperatures except for V_3 which is converted to reflected radiant emittance by Equation 9. The corrections for the contribution of the thermal emission from the quartz window and housing to the irradiance of the detector are discussed later.

Time Constant Measurements

The time response of the detectors was measured by using the array of tungsten bulbs described above. The radiometer was placed to view the white diffuse paper through the quartz window. The bulbs were turned on until the detectors attained an equilibrium response, and the bulbs were then turned off. The temperatures of the quartz window and the radiometer housing, as well as that of each detector network, were continuously recorded as a function of time until the changes became negligible. Figure 14 shows the results of such a measurement with the detector temperature differences plotted as a function of time for a housing temperature of about -20°C. The black and white detectors have very nearly the same time response and show the characteristic exponential rise and decay with time. These results give a value for the time constant of about 35 sec for the rise portion of the graph under the conditions of detector equilibrium temperature shown. The decay portion was not used in determining the time constant because the effects from the heating of the quartz window by the tungsten bulbs were judged to be too large.

Calibration of the Radiometer Components

Several other measurements were performed by the manufacturer which are necessary for the interpretation of the instrumental response. These consist of temperature-resistance

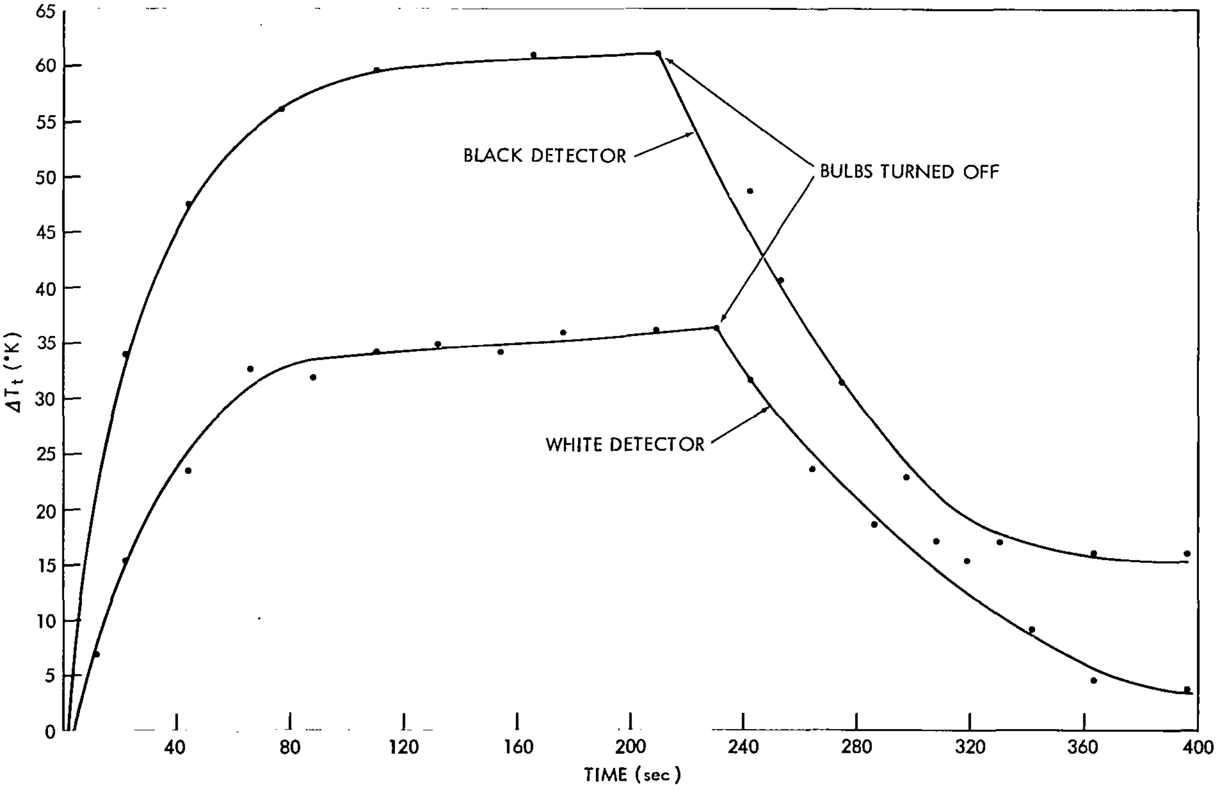

Figure 14—Detector time constant determination for the low resolution radiometer. The time constant is determined from the rise portion of the curve. The housing temperature was about -20°C.

calibrations of the detectors, sensistors, and other thermistors used in the radiometer. Figure 15 shows the sensistor response curves as a function of temperature. The sensistor resistance values are $S_i = S_1$; $S_j = S_2$ for the black detector and $S_i = S_4$, $S_j = S_3$ for the white detector. Figure 16 shows an example of the thermistor detector response as a function of temperature for the black and white detectors. Curves of the type shown in Figures 15 and 16 were used for the reduction of network resistance data to the required thermistor detector temperatures.

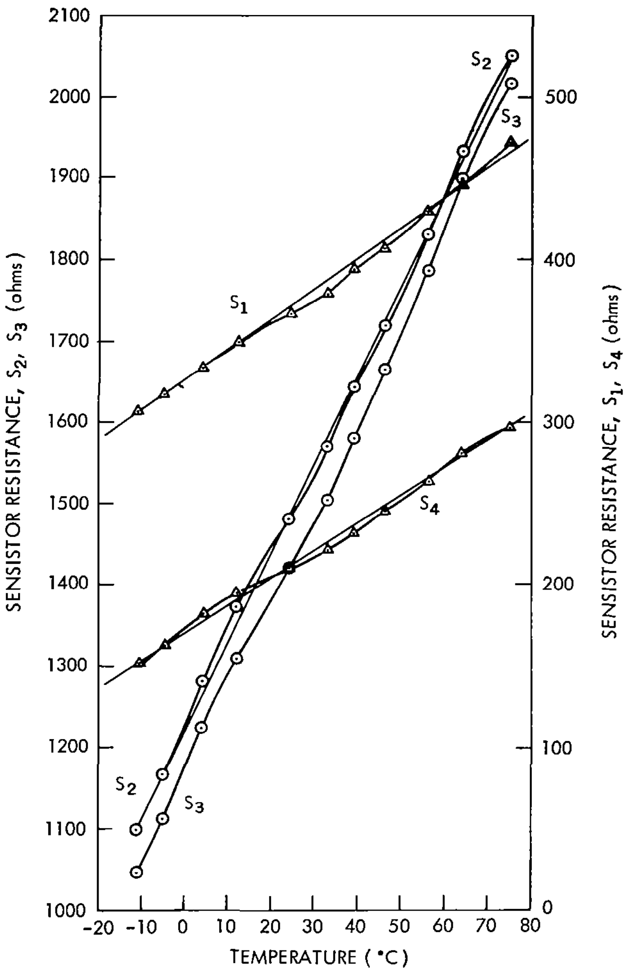

Figure 15—Sensistor response as a function of temperature.

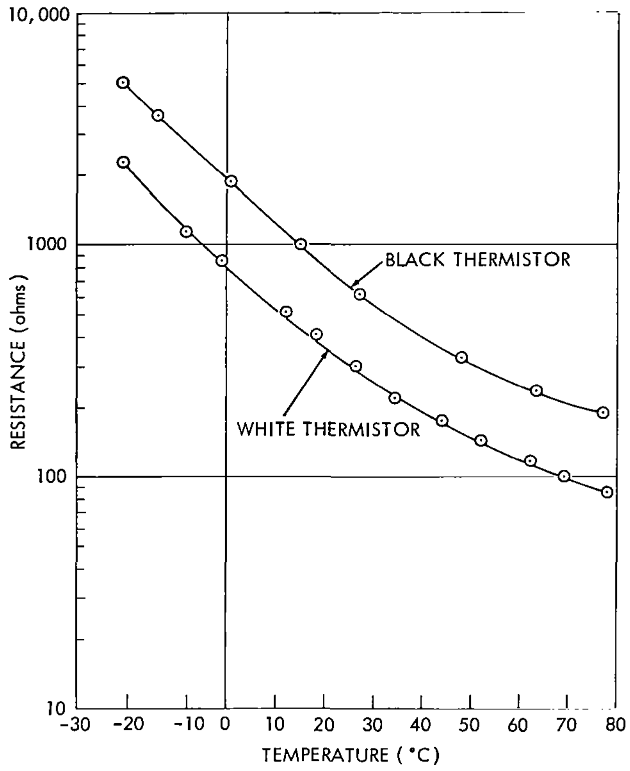

Figure 16—Black and white thermistor detector response as a function of temperature.

Subcarrier Oscillator Calibration

Generally, the resistance-controlled subcarrier oscillator used in the radiometer calibration was not flown in the satellite, and so a separate calibration for the flight oscillator was necessary. This calibration consisted of measuring the output frequencies and input resistances, with the temperature of the oscillator T_E as a parameter. A decade box was used to simulate the input resistances. The calibration curve for an oscillator is shown in Figure 17.

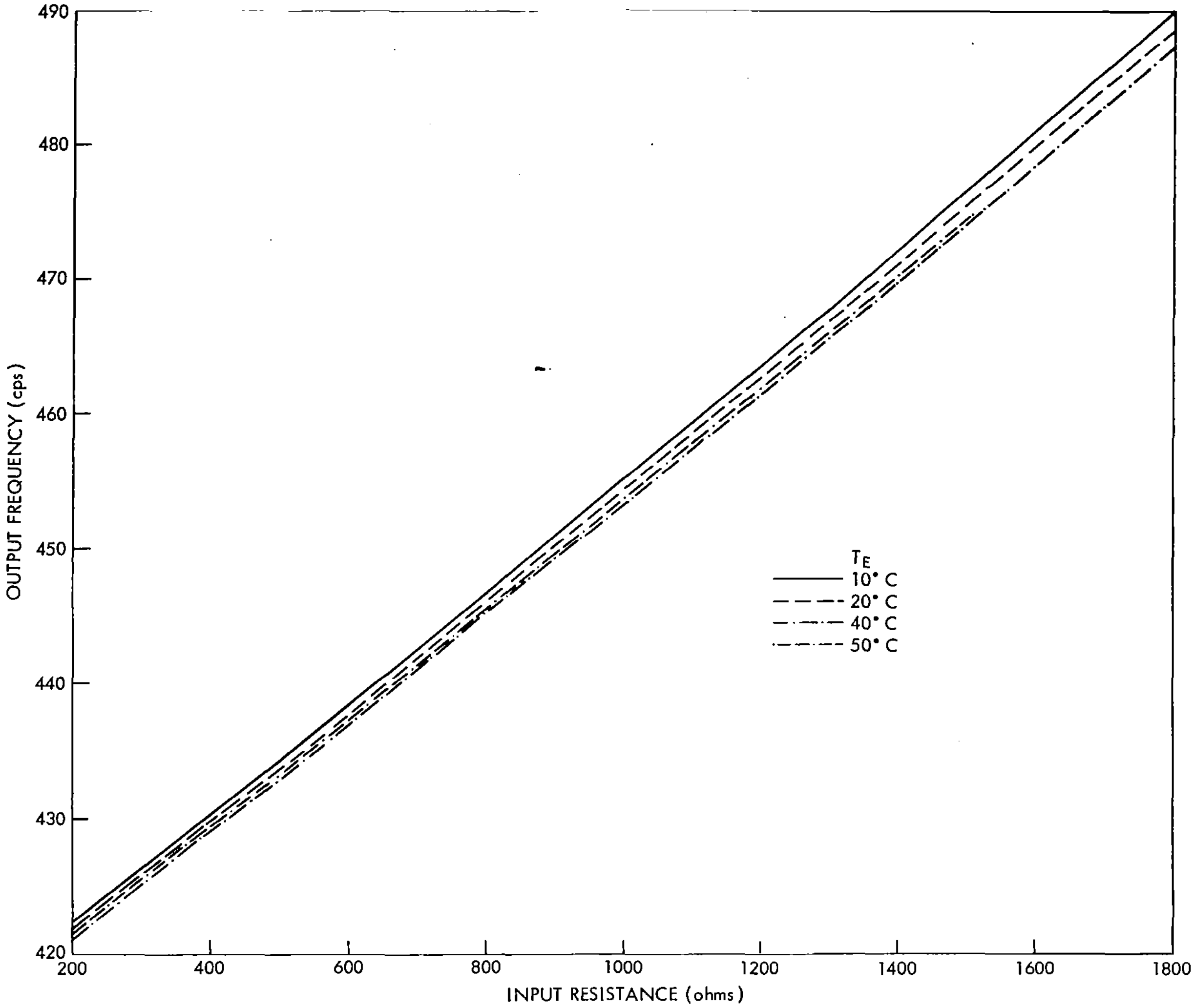

Figure 17—Resistance-controlled subcarrier oscillator calibration curve. The temperature of the oscillator is shown as a parameter.

Additional Measurements

In addition to the individual radiometer calibration measurements, other measurements were performed to check, in general, the field of view, the spectral response of radiometer components, the spectral distribution of bulbs, and the degradation of spectral response due to exposures of ultraviolet radiation.

The field of view measurements were performed by the manufacturer. These were made by linearly traversing a point source of light across the field of view and measuring the radiometer response as a function of angle of the source from the optical axis. Results from such a measurement are shown in Figure 18. As was mentioned previously, the field of view of each detector is

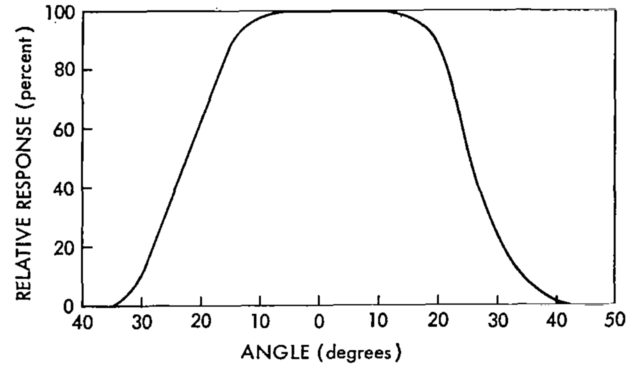

Figure 18–Field of view of the low resolution radiometer.

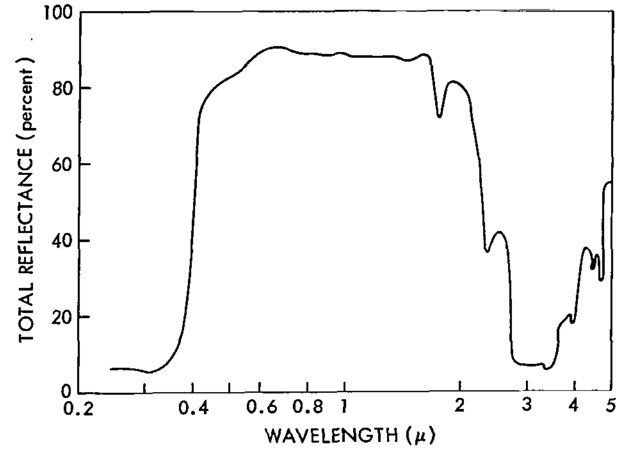

Figure 19—Spectral reflectance of the white coating used on the thermistor detector for the region 0.2 to 3.5μ. The sample was 30μ thick on a backing of pure SiO_2. The portion of the curve beyond 3.5μ is beyond the limits of the spectrophotometer used in making the measurements.

a function of the angular aperture of the cone and also the ratio of cone length to detector radius. The measurement shown in Figure 18 gives a field of view of about 45 degrees or 0.6 steradian at the half-power points.

Spectral response measurements for the white paint coating are shown in Figure 19. The measurements were performed by the manufacturer using a Beckman DK-2 spectrophotometer for the spectral range from 0.2 to 3.5μ. The average total reflectance for this region, with the solar irradiance curve of Johnson (Reference 6) as a weighting function, is 77 percent. Reid and McAlister (Reference 7) have made measurements (Figure 20) on a similar white paint in the region of 2 to 15μ which show that the reflectance of the white paint in the region of 3.5 to 5.5μ is high. However, only 1.5 percent of the sun's total energy and 2.5 percent of the energy of a 300°K blackbody fall in this region, and these high reflectance values, therefore, are not critical to the measurements. Approximately 55 percent of the energy of a 300°K blackbody falls in the spectral region from 5.5 to 15μ where the reflectance varies between 5 and 10 percent. At wavelengths greater than 15μ, where 43 percent of the 300°K blackbody energy lies, no reflectance values are available.

The white paint coating was exposed to an ultraviolet source which would show whether

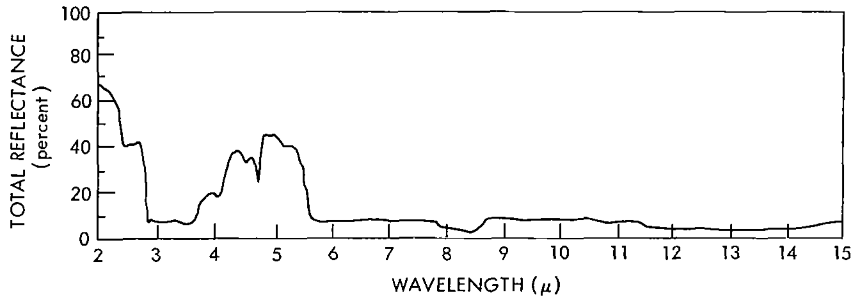

Figure 20—Spectral reflectance of a white paint similar to that used for Figure 19 for the region 2 to 15μ.

any degradation of reflectance occurred. The paint samples were exposed to about 5 times the solar flux in the spectral region from 2000 to 4000A for various exposure times. Figure 21 shows the original solar reflectance of the white paint and the degradation effects of direct exposure to 25, 76, and 214 equivalent solar hours. The Tiros II and IV low resolution radiometer lifetimes were both approximately 1300 orbits and during this time each radiometer viewed the earth for about 430 hr. For an assumed mean earth albedo of 10 percent in this near-ultraviolet region, the equivalent solar exposure was about 43 hr. The exposure for Tiros III was considerably longer. Hence, long term changes in spectral response can be expected to occur during a radiometer's lifetime.

Figure 22 shows the spectral reflectance of the aluminized mylar cone. In general, the reflectance decreases with decreasing wavelength. The diffuse spectral reflectance of the white paper which was used in the reflected solar radiation calibration, is shown in Figure 23. From 0.3 to 0.5μ the reflectance increases, from 0.5 to 1.3μ it is uniform, and from 1.3 to 2.8μ it decreases. The energy distribution of the blue photoflood bulbs is shown in Figure 24. The peak of the distribution occurs at 1.25μ which corresponds to a blackbody temperature of 2300°K. The deviation of the energy distribution in the region of 0.7μ, from that of a blackbody function for a tungsten filament of 2300°K, is due to the peculiar transmission properties of the blue envelope of the bulbs in this region. The deviation from a blackbody distribution at the long wavelength region is due to the lower transmittance of the glass envelope.

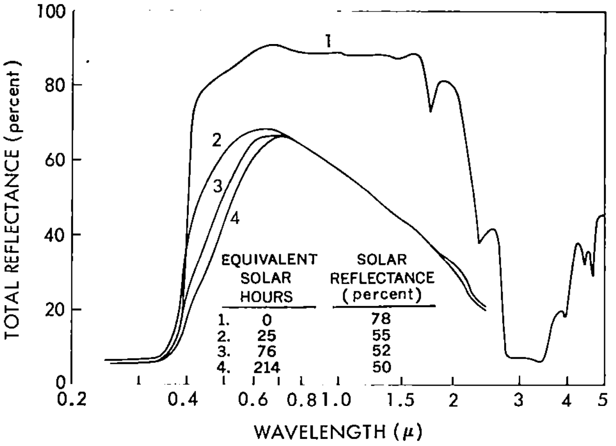

Figure 21—The ultraviolet degradation of the white paint after 25, 76, and 214 equivalent solar hours of ultraviolet exposure. The reflectance values were averaged by using the solar irradiance curve from Johnson (Reference 6) as a weighting function.

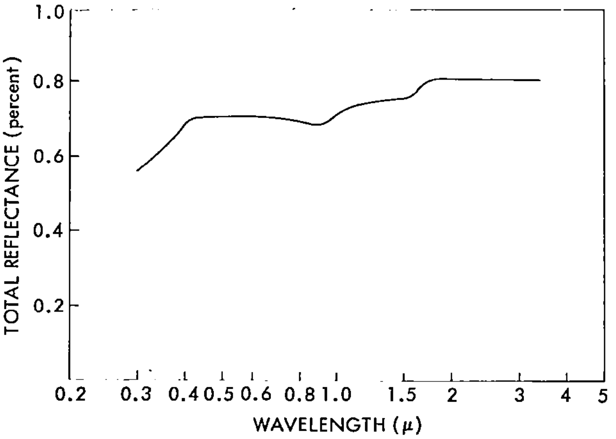

Figure 22—Spectral reflectance of the cone of the low resolution radiometer for the region 0.3 to 3.0μ.

The spectral response $\phi(\lambda)$ of the radiometer was assumed to be fairly constant with wavelength in the spectral region of 0.2 to 2.5μ. This assumption is equivalent to the radiometer response being proportional to the total energy of the source regardless of the source spectral distribution, as long as the bulk of the energy output falls in the above region. The spectral response of the radiometer $\phi(\lambda)$ is proportional to the product $R_c(\lambda)\ \alpha_t(\lambda)$, where $R_c(\lambda)$ is the spectral reflectance of the reflecting cone and $\alpha_t(\lambda)$ is the spectral absorptance of the painted

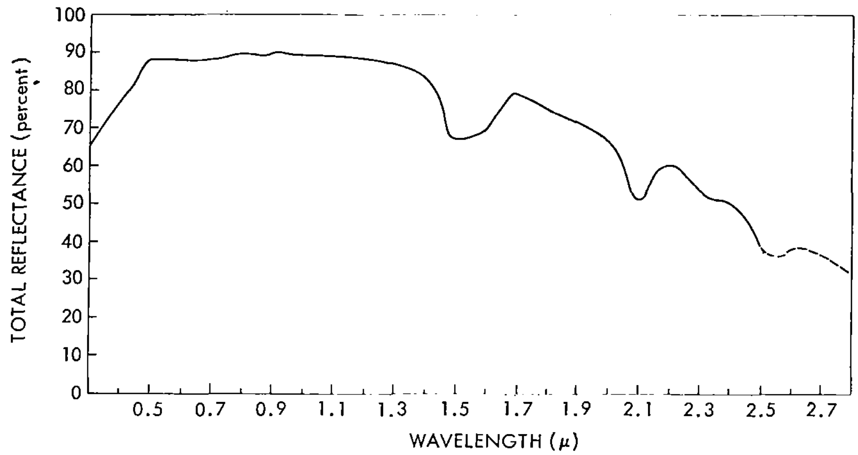

Figure 23—Spectral diffuse reflectance of the white paper used in the reflected solar radiation calibration.

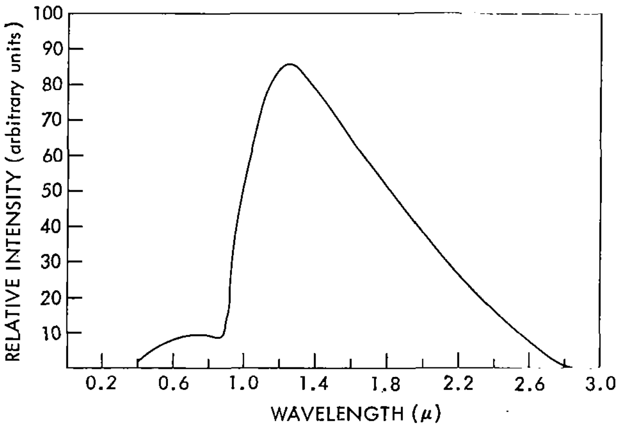

Figure 24—Relative intensity of the blue photoflood bulbs used in the reflected solar radiation calibration. The energy peak is at 1.25μ which corresponds to a blackbody temperature of 2300°K.

thermistor detector. It is assumed that $\alpha_t(\lambda) = 1 - R_p(\lambda)$, where $R_p(\lambda)$ is the spectral reflectance of the paint coating on the thermistor detector. If the paint coating is too thin this will be a bad assumption. For comparison purposes an auxiliary spectral response function $\phi'(\lambda)$ will be considered which is defined by $\phi'(\lambda) = \phi(\lambda)\, r_p(\lambda)$. The diffuse reflectance of the white paper is included because of its effect on the spectral energy distribution of the source. The above definition is somewhat arbitrary and the $r_p(\lambda)$ could have been included as part of the sources, but for the comparison to be presented, the above definition will be used. The reflectance of the black paint is assumed to be zero for all wavelengths. The auxiliary spectral response functions pertaining to the black and white detectors are now

$$\phi_b'(\lambda) = r_p(\lambda)\, R_c(\lambda) ,$$

$$\phi_w'(\lambda) = r_p(\lambda)\, R_c(\lambda) \left[1 - R_p^w(\lambda)\right] .$$

The functions $r_p(\lambda)$, $R_c(\lambda)$, and $R_p^w(\lambda)$ have been shown in Figures 19, 20, 22, and 23. The functions $\phi_b'(\lambda)$ and $\phi_w'(\lambda)$ are shown in Figure 25. The energy distribution for the photoflood bulbs and the solar irradiance curve for zero air mass by Johnson (Reference 6) are also shown in

Figure 25. The peak intensities of the two curves are normalized to the same value. As can be seen from the $\phi'(\lambda)$ curves of Figure 25, the assumption of a flat spectral response is not very good near the upper and lower wavelength limits of $\phi_b'(\lambda)$ and $\phi_w'(\lambda)$. However, to a first approximation a suitable mean value for $\phi_b'(\lambda)$ and $\phi_w'(\lambda)$ may be selected. The deviation of $\phi_w'(\lambda)$ from its mean is most pronounced for wavelengths shorter than 0.4μ. Since less than 10 percent of the solar energy lies in this region, the first approximation is still reasonable. Figure 25 indicates that since $\phi_w'(\lambda)$ and $\phi_b'(\lambda)$ are not constant, the radiometers should be calibrated spectrally.

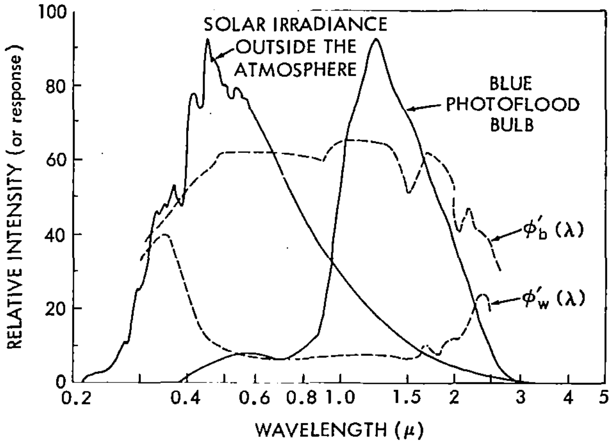

Figure 25—The spectral response curves pertaining to the black and white detector are shown along with the solar irradiance curve from Johnson (Reference 6) and the relative intensity curve for the blue photoflood bulbs.

Sources of Error

The sources of error in the calibration are numerous and difficult to evaluate numerically in terms of both random and systematic effects. The net result of these errors manifests itself in the accuracy to which the coefficients of the energy balance equations can be determined.

The precision (random error) of temperature measurements of the calibration is considered to be ±1.0°K for T_t and ±0.5°K for T_s and T_e. These result from the various conversions from resistance to temperature. The dispersion of T_t also includes a random error caused by the method of measuring resistances via frequency readings from the subcarrier oscillator. The oscillator used during calibration has a small local variation about its mean calibration curve. The calibration curve also drifts slowly in time but this systematic effect is largely eliminated since the frequency to network resistance conversions (via the decade box) are made immediately after the measurement.

The accuracy (systematic error) of the calibration is considered to be ±2.0°K for T_t and ±1.0°K for T_s and T_e. Some of the inherent inaccuracies of the calibration arise in the apparatus used to measure and record the various temperatures. The measuring devices have been described in the calibration section. In the thermal calibration, the cavity and housing temperatures are maintained by circulating liquids. Any gradient between the temperature of the point of measurement and the controlling temperature may cause a systematic error. It is also quite possible that the temperature difference would consist of random fluctuations and thus contribute to the random error.

The reflected solar radiation portion of the calibration is subject to considerably greater error than the thermal part. This is partially due to the greater number of intermediate measurements required; in addition, the types of measurements are inherently subject to greater error.

The various sources of error (without regard to the random or systematic effect) are discussed below.

The white diffusely reflecting paper was assumed to be a Lambert's Law surface and later measurements indicate a slight departure from this law for large angles of incidence. For this reason, and also to avoid any specular reflectance components, large angles of incidence were avoided.

Because the field of view of the thermopile is smaller than that of the radiometer, it is necessary to irradiate the paper uniformly so that the radiometer and thermopile observe the same radiant emittance. The large field of view of the radiometer requires that the surface area of the paper be large; it becomes difficult to produce a uniform irradiance over the entire surface area. In addition, it is difficult to maintain a uniform irradiance because the bulb voltages are not controlled accurately and because the bulbs deteriorate at different rates, thereby causing asymmetries in the bulb outputs.

The radiometer views the paper through the quartz window of the vacuum chamber. The window cannot be cooled to eliminate or minimize its thermal emission since frosting begins to appear. Hence, during the tests, the window is usually left at room temperature and any slight changes in its temperature due to absorption of infrared energy by the window from the bulbs is monitored by a thermocouple. The quartz temperature is measured before, half-way through, and after the test. A correction is made for the quartz thermal emission contribution to the detectors and the only error due to this effect would be the error in the quartz temperature measurement.

Reduction of the Calibration Data

The network resistance R_N must be converted to detector temperature T_t before the coefficients for the heat transfer equation can be evaluated. This conversion is illustrated by the portion of the flow diagram of Figure 26 enclosed by the dashed lines. The portion of the flow diagram outside the dashed lines will be discussed later. S_i and S_j , which are functions of the housing temperature, are manually determined as part of the input to an electronic computer program which reduces the network resistance to detector resistance via Equation 3. The other input element of the computer program is R_N . The computer output is the detector resistance which is manually converted to the detector temperature.

DETERMINATION OF THE COEFFICIENTS OF THE HEAT TRANSFER EQUATION

The coefficients of the heat transfer equation of each detector are determined from the calibration data. The heat transfer equation used in the determination of the coefficients is Equation 2 with the conduction term omitted. The coefficients are determined by the method of least squares and the resulting set of normal equations is solved simultaneously by using Cramer's rule for the desired coefficients. This type of solution must be checked carefully to insure that the coefficients are not affected by normal equations closely approaching dependency and creating a solution which is nearly indeterminate. The radiative and conduction coefficients are evaluated from the thermal calibration data, and the reflected solar radiation coefficient from the reflected solar radiation calibration data.

Thermal Coefficients

The thermal calibration data, in terms of temperature, are shown in Figure 27 for the black detector of the Tiros IV radiometer. For the appropriate values of the constants k_1, k_2, and k_2', a least squares method was first applied to the thermal portion of the heat transfer equation (2):

$$T_t^4 = k_1 T_e^4 + k_2 T_s^4 + k_2' \left(T_s - T_t\right) \qquad (10)$$

In applying the least squares method the variable whose residual error is to be minimized must be chosen. The conventional choice is the variable which is to be predicted $\left(T_e\right)$ under the assumption that the errors in the other measured quantities $\left(T_t , T_s\right)$ are small. This was not done in the present case since the T_e measurement is fairly accurate with respect to T_t. Therefore, the residual error of T_t was minimized in these calculations.

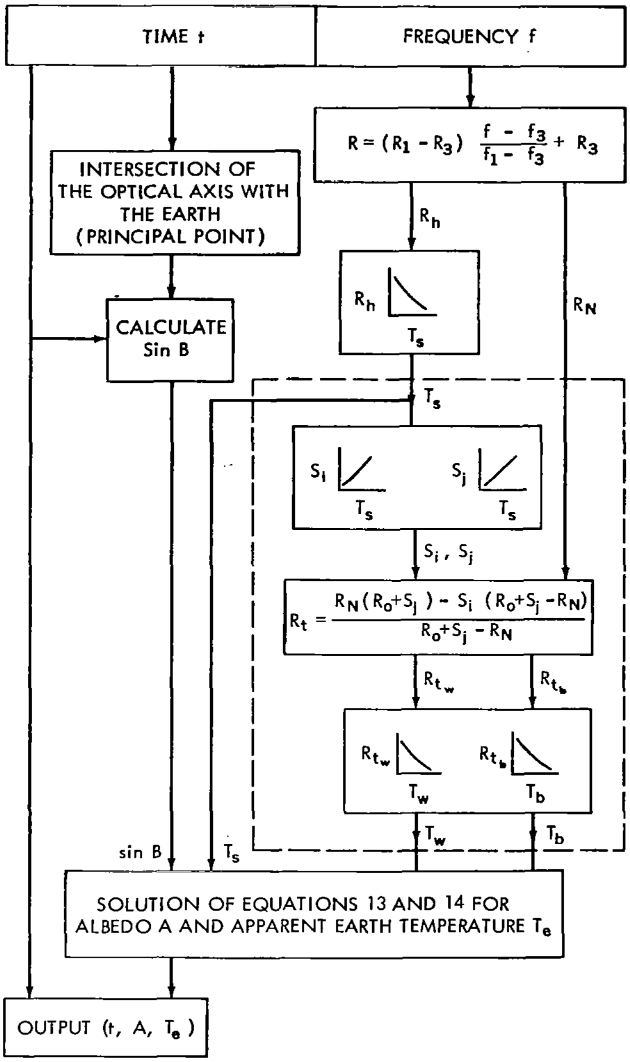

Figure 26—Flow diagram for reduction of the low resolution radiometer data.

In Equation 10 no acceptable solution of the 3 normal equations was obtained because of the unavoidable loss, through subtraction, of the 3 or 4 leading significant figures in the expressions for the k's. The loss of significant figures reflects the nearly indeterminate state of the solution. As the input temperatures are only significant to three figures, the resulting k's cannot be considered reliable. The cause for the unreliability of the coefficients, in terms of the three nearly linearly dependent normal equations, is that instead of one unique solution for the coefficients, an infinite number of solutions for the normal equations exist in this nearly indeterminate situation. Therefore, a different method of solution for the coefficients must be employed or the heat transfer equation must be altered so that the least squares solution becomes more determinate.

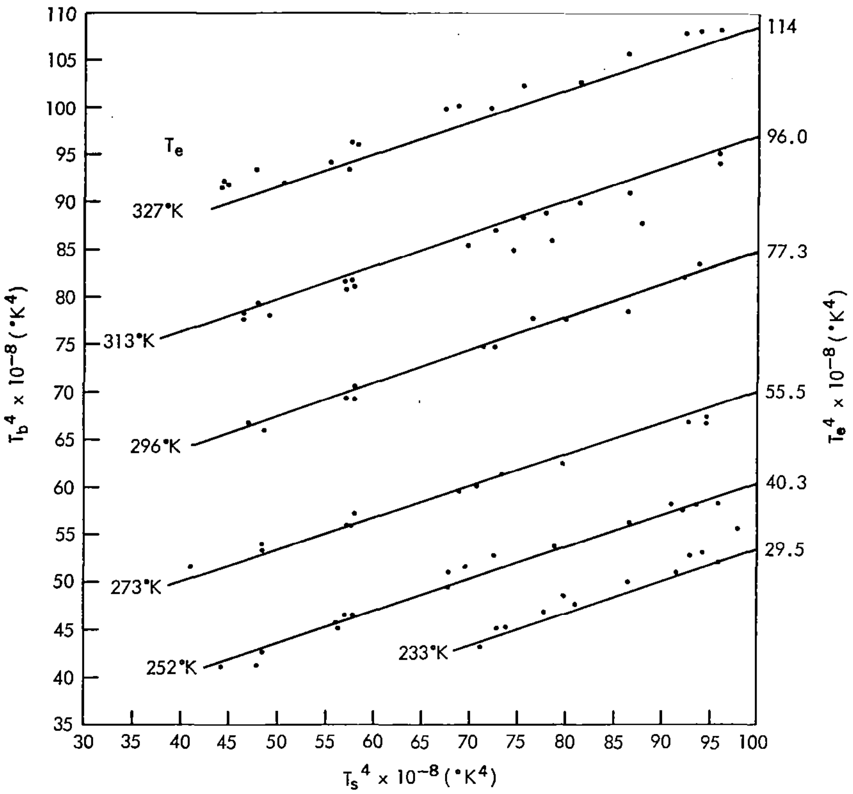

Figure 27—Thermal calibration data and least squares solution (solid lines) used in determining thermal coefficients for the black detector of the low resolution radiometer on Tiros IV. The apparent earth blackbody temperature is the parameter for the various curves.

If the conductive term of the heat transfer equation is neglected, Equation 10 becomes

$$T_t^4 = k_1 T_e^4 + k_2 T_s^4 \ . \tag{11}$$

Mathematically, the conductive term is ignored but physically the conductive effects are absorbed in the values of k_1 and k_2. The solution of the two normal equations for this case involves the loss of only one or two significant figures and yields coefficients that approximate the physical situation. In Figure 27 the least squares solution for all the data points is indicated by the solid line. The coefficients for this solution and their estimated probable errors are

$$k_{1b} = 0.65 \pm 0.02 \ ,$$

$$k_{2b} = 0.34 \pm 0.02 \ .$$

A similar solution for the white detector of Tiros IV gives

$$k_{1w} = 0.51 \pm 0.02 \ ,$$

$$k_{2w} = 0.49 \pm 0.02 \ .$$

Table 2

Tiros III and IV Low Resolution Radiometer Coefficients.

Satellite	k_{1b}	k_{2b}	$k_{3b}\left(\frac{°K^4\ cm^2}{watt}\right)$	k_{1w}	k_{2w}	$k_{3w}\left(\frac{°K^4\ cm^2}{watt}\right)$
Tiros III	0.60	0.39	1210×10^8	0.51	0.44	807×10^8
Tiros IV	0.65	0.34	2214×10^8	0.51	0.49	1153×10^8

The thermal coefficients for Tiros IV, and also those of Tiros III, are listed in Table 2. The higher value of k_{1b} with respect to k_{1w} indicates that in the infrared the black detector has a greater average spectral absorptance than the white detector. The k_1's are lower and the k_2's higher than called for by design with the consequence that the thermal coupling between the detector and the satellite is fairly strong compared with the coupling between the detector and the earth. The detector temperature is therefore strongly influenced by the satellite temperature. The least squares probable errors are $\pm 0.9 \times 10^8\,°K^4$ for T_b^4 and $\pm 0.7 \times 10^8\,°K^4$ for T_w^4. The probable errors for T_b and T_w are ±0.9°K and ±0.7°K, respectively.

An attempt was made to estimate the conduction constant k_2' by using a unique solution for a given T_e curve. The expression for k_2' consists of terms such as $\left(T_{t_i}^4 - T_{t_j}^4\right)$ and $\left(T_{s_i} - T_{t_i}\right)$. If the probable error in T_t is ±1.0°K the percentage error in the term $T_{s_i} - T_{t_i}$ varies from 4 to 20 percent as $T_{s_i} - T_{t_i}$ varies from 2.5°K to 5°K. Under these conditions k_2' depends on the difference of quantities containing considerable error and no accurate value can be determined.

In summary, the evaluation of the thermal coefficients indicates that a representative value for the conduction coefficient cannot be determined. The optimum heat transfer equation for the detectors is considered to be Equation 11 and the best values for the thermal coefficients for Tiros III and IV are listed in Table 2. As the thermal coefficients are in part functions of $R_c(\lambda)$ and $\alpha(\lambda)$, improvement of the values of the coefficients to meet design specifications involves increasing $R_c(\lambda)$ and $\alpha(\lambda)$ in the infrared.

Reflected Solar Radiation Coefficient

The reflected solar radiation coefficient k_3 is determined from the energy balance equation for the detector:

$$T_t^4 - \left(k_1 T_q^4 + k_2 T_s^4\right) = k_3 S A \sin B \qquad (12)$$

The term $\left(k_1 T_q^4 + k_2 T_s^4\right)$ is the correction for thermal effects of the quartz window and radiometer housing during the calibration. Because the quartz window is nearly opaque to thermal radiation, the thermal contributions to the irradiance of the detector are felt to be due to the quartz window and the radiometer housing only. T_q, T_t, T_s, and the term $S A \sin B$ are obtained from the reflected solar radiation calibration, and the coefficients k_1 and k_2 have been determined previously, leaving k_3 as the only unknown in the equation. $S A \sin B$ is determined by Equation 9. The Tiros IV reflected solar radiation calibration data are shown in Figure 28. A least squares fit used to find the values for k_3 gives k_{3b} = (2214 ± 114) × 10^8 °K^4-cm^2/watt and k_{3w} = (1153 ± 68) × 10^8 °K^4-cm^2/watt. The magnitude of k_{3w} with respect to k_{3b} indicates that the reflectance of the white paint is poor in the visible region. The percentage error in k_3 is 5.2 and 5.9 percent for the black and white detectors, respectively. The least squares probable error in $\left[(T_t^4) - (k_1 T_q^4 + k_2 T_s^4)\right]$ is ±2.9 × 10^8 °K^4 for the black detector and ±1.7 × 10^8 °K^4 for the white detector. In the visible region, some indication of the spectral absorptance of the black detector relative to that of the white detector is given by the ratio of their relative response (k_{3b}/k_{3w}) which is only 1.9.

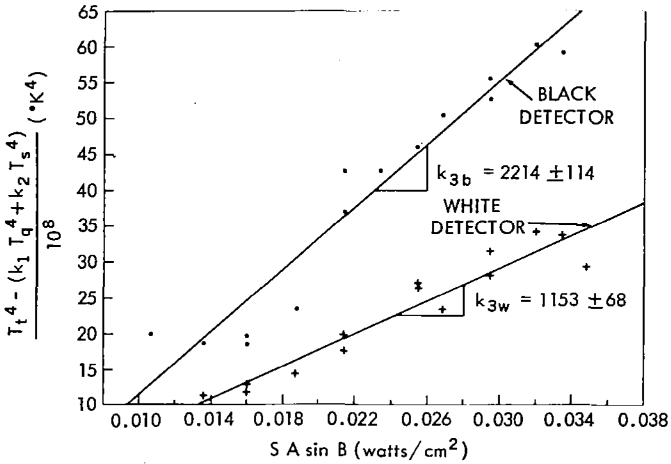

Figure 28—Reflected solar radiation calibration data and least squares solution (solid lines) used to determine reflected solar radiation coefficients for the black and white detectors of the low resolution radiometer of Tiros IV.

The reflected solar radiation coefficients for the Tiros III and IV wide field radiometers are listed in Table 2. A comparison of the coefficients indicates a large difference between the numerical k_3 values for Tiros III and IV. The values are 1210 × 10^8 °K-cm^2/watt vs. 2214 × 10^8 °K-cm^2/watt for k_{3b} and 807 × 10^8 °K-cm^2/watt vs. 1153 × 10^8 °K-cm^2/watt for k_{3w}. The difference is due either to different calibration conditions or a different spectral response between radiometers. The calibration conditions which could vary are the reflectance of the paper, the transmittance of the quartz window, or the color distribution of the photoflood bulbs. If any of the above variations did occur, it is not likely that the magnitude of the variation would be large enough to cause the observed differences. A difference in the spectral response for the two radiometers would be a more reasonable explanation since k_3 is, in part, a function of $R_c(\lambda)$ and $\alpha(\lambda)$ in the visible region. Since $\alpha(\lambda)$ should be fairly constant in the visible region, especially for the black detector, it would seem that the cone reflectance is responsible for this effect. This was borne out by an inspection of several other radiometers, which showed large variations in the thicknesses of the aluminum coatings, some being partially transparent.

DATA PROCESSING AND REDUCTION

The telemetry of data from the satellite has been previously described (Reference 8). The designated bandwidth for the telemetry of the low resolution radiometer information is 425 to 475 cps (designated channel 6). The resistance-controlled, phase-shift subcarrier oscillator for channel 6, with output frequency nearly linear with respect to input resistance, converts the input resistances to frequencies. Channel 6 is a time-sharing channel, the time sharing controlled by a mechanical commutator which switches the appropriate resistor into the oscillator for a 6 sec sampling period. There are 5 commutated subchannels and the fifth includes a group of 7 to be subcommutated. Included in the first 4 commutations are the wide field sensor data and the radiometer housing temperature data. The fifth commutation includes resistances which represent environmental temperatures, instrumentation cannister pressure, and fixed resistor telemetry calibrations. The latter consist of fixed resistors near the lower (R_3) and upper (R_1) limits of the bandwidth which give reference points for calibration of the channel 6 frequencies. The oscillator converts the input resistance into output frequency signals which are amplified and recorded on a magnetic tape located in the satellite. A block diagram of the satellite instrumentation is shown in Figure 29. Upon interrogation of the satellite, the tape signal is telemetered to the acquisition station and recorded on magnetic tape. This tape is sent to the ground station where it is demodulated and decommutated. The demodulation and decommutation process is illustrated in Figure 30. The data are now in analog form in terms of frequencies. A typical analog record is presented in Figure 31.

The frequencies are read directly from the analog record with a Gerber Semi-Automatic Analog to Digital Conversion System. The analog-to-digital conversion is made by a digital voltmeter whose output is fed through a Flexowriter to produce a punched tape output. This tape serves as an input for an LGP-30 computer program. Variable calibration is provided by the Gerber System through the use of zero offset and scale factor controls. As long as the analog frequency output remains linear, within the frequency interval encompassed by the fixed resistors, the analog readings can be made

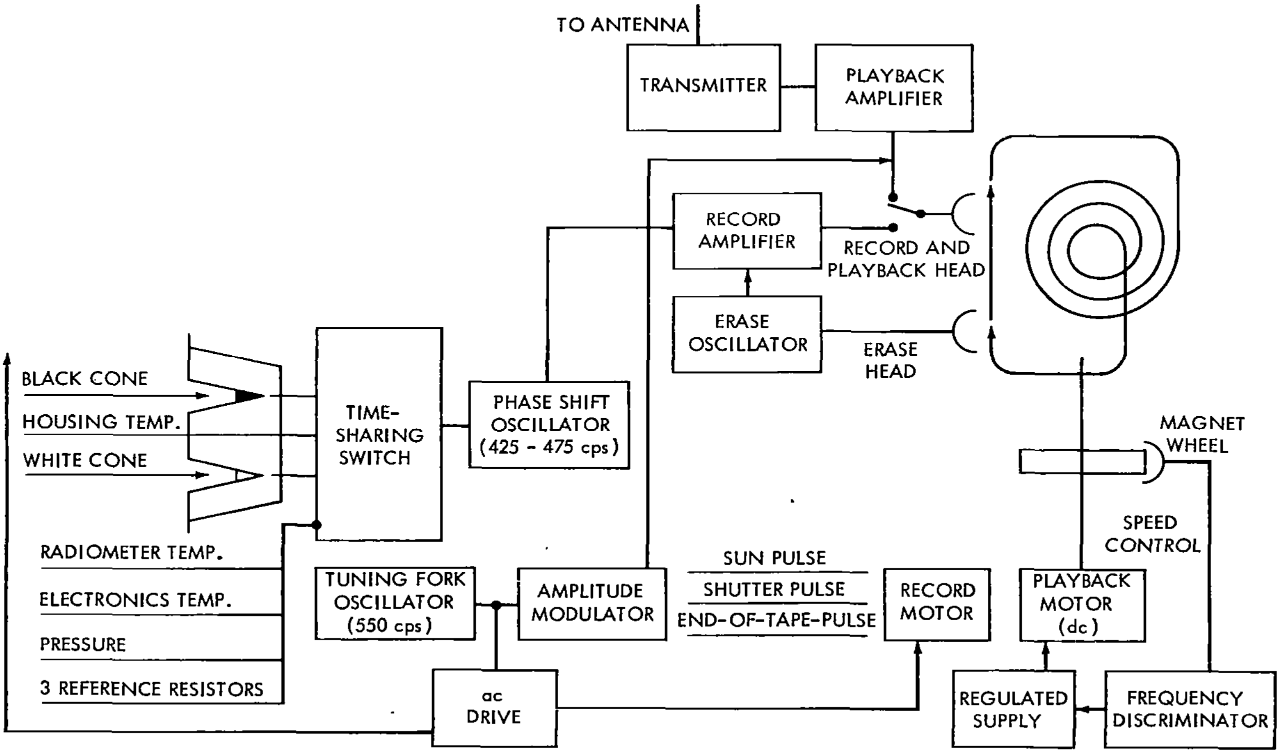

Figure 29—Block diagram of the satellite instrumentation used by the low resolution radiometer.

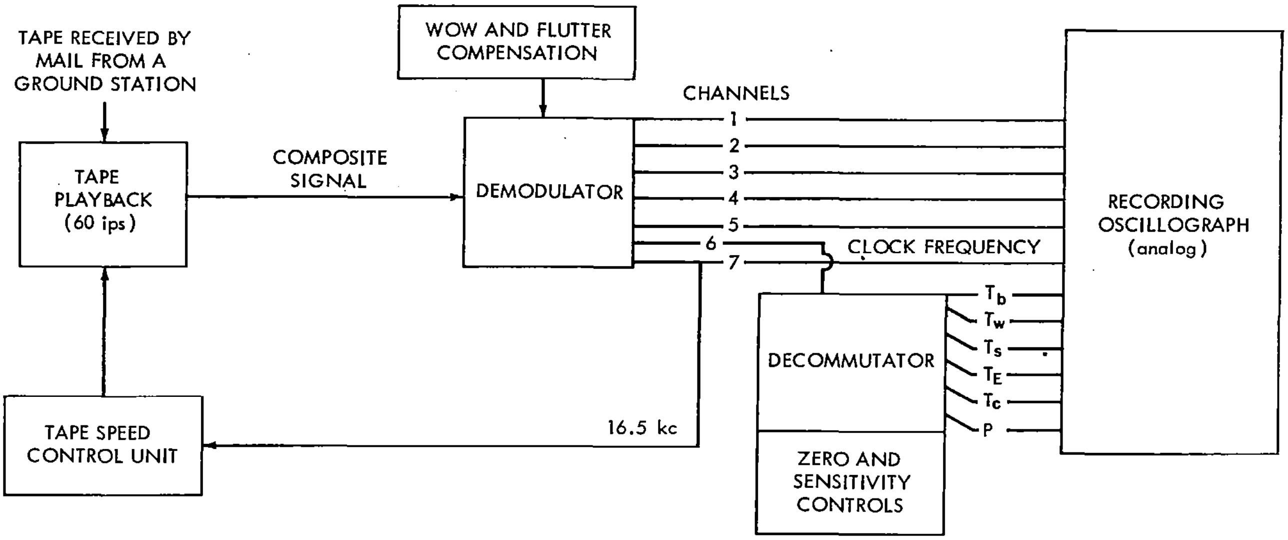

Figure 30—Block diagram of the information flow at the data processing center in producing the radiation data of the low resolution radiometer and of the five medium resolution channels in analog form. The output of the decommutator consists of temperatures of the black and white detectors, three environmental temperatures, and the canister pressure P.

in terms of frequency. The frequency readings are taken as a function of time which is also entered on the punched tape. The reduction of frequencies to T_e and A is illustrated in the flow diagram of Figure 26. Under the assumption that the frequency vs. resistance curves (with T_E as a parameter) are linear, the conversion from frequency to resistance is made by the following equation:

$$R = \left(R_1 - R_3\right) \frac{f - f_3}{f_1 - f_3} + R_3 .$$

The portion of the flow diagram used for conversion of resistances to temperatures has already been discussed. The temperatures can now be introduced into the heat transfer equations for the black and white detectors and the simultaneous solution of these two equations yields T_e and A. The computer output gives T_e and A as a function of time. The expressions for A and T_e are

$$A = \frac{k_{1w} T_b^4 - k_{1b} T_w^4 + \left(k_{2w} k_{1b} - k_{2b} k_{1w}\right) T_s^4}{\left(k_{3b} k_{1w} - k_{3w} k_{1b}\right) S \sin B} , \tag{13}$$

$$T_e^4 = \frac{k_{3b} T_w^4 - k_{3w} T_b^4 - \left(k_{3b} k_{2w} - k_{3w} k_{2b}\right) T_s^4}{k_{3b} k_{1w} - k_{3w} k_{1b}} . \tag{14}$$

As can be seen from the channel 6 sequencing, four commutated measurements exist between an individual sensor temperature sampling, so that T_e and A can be determined every 30 sec. The albedo must be corrected for the angle of solar incidence for every satellite position.

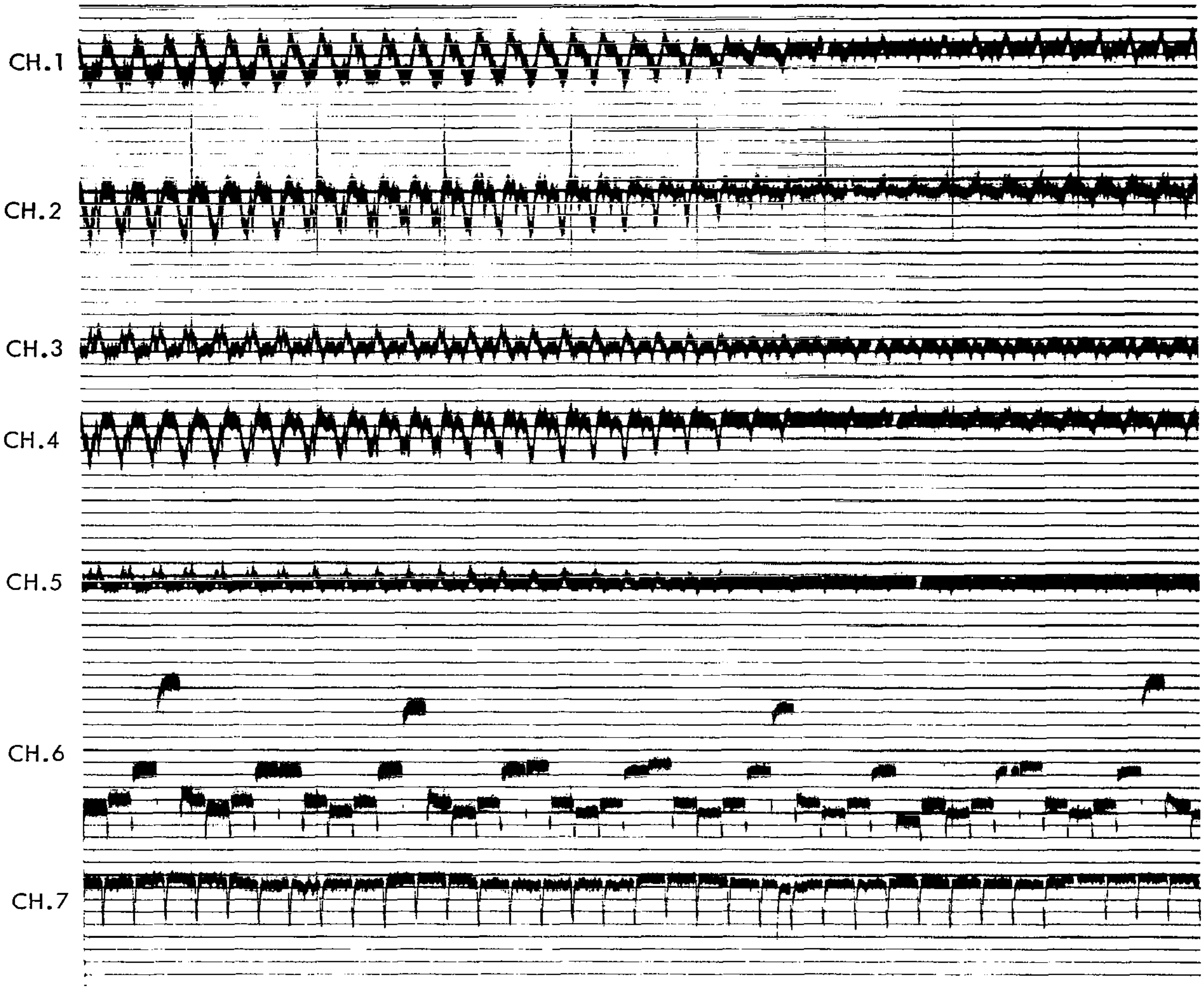

Figure 31—Oscillogram showing all channels of the radiometer experiment. They are, from top to bottom, the five medium resolution channels in numerical order, the commutated channel 6, and the envelope of the clock frequency showing sun sensor pulses.

The orbital data provide the time-correlated geographic location of the intersection of the spin axis with the earth. Since this intersection is also, practically speaking, the center of the low resolution radiometer field of view, the radiometer data are geographically located as a function of time.

Because of instrumental and calibration difficulties, only selected orbits of Tiros II low resolution data have been reduced. Since both the low resolution radiometer and the University of Wisconsin experiment are recorded on the commutated channel 6 of Tiros III and IV, it has been found convenient to program the reduction of their data simultaneously on a CDC-1604 computer at the University of Wisconsin. This program is now in the final stages of checkout, and further results and conclusions must await its completion.

Selected orbits of Tiros III low resolution data have been reduced by the method described in the last section and presented in the literature (Reference 9). One of these orbits (43) will be presented here as an example of the reduced data. The geographic location of the orbit considered is over North Africa with the radiometer viewing area passing from the cloudless Mediterranean Sea over the Libyan Desert to the tropical regions of the Sudan. Figure 32 illustrates the observed equilibrium detector temperatures, the observed radiometer housing temperature, and the resultant apparent earth temperature and albedo as a function of time. The values of T_e and A were calculated from the detector and housing temperatures indicated by the individual points and they show considerable scatter. The broad spectral response and relatively long time constant of the radiometer would indicate that the curves for albedo and earth temperature are slowly changing functions similar to the curves for the detector temperatures. In general, the predicted apparent earth temperature curve would approach the mirror image of the albedo curve. However, it is evident from Figure 32 that sharp fluctuations do exist in the values for T_e and A. These fluctuations are introduced by the radiometer, as will be shown below. In an effort to smooth the T_e and A fluctuations, curves were drawn to smooth the data points of detector temperature and housing temperature; these curves are also shown in Figure 32. The results for T_e and A shown in Figure 33 were calculated from the smoothed curves of detector and housing temperatures.

In order to gain some insight into the fluctuations of T_e and A, their total differentials and probable errors have been calculated. The total differentials for A and T_e are

$$dA = \frac{\partial A}{\partial k_{1b}} dk_{1b} + \frac{\partial A}{\partial k_{2b}} dk_{2b} + \cdots + \frac{\partial A}{\partial T_s} dT_s \cdots , \qquad (15)$$

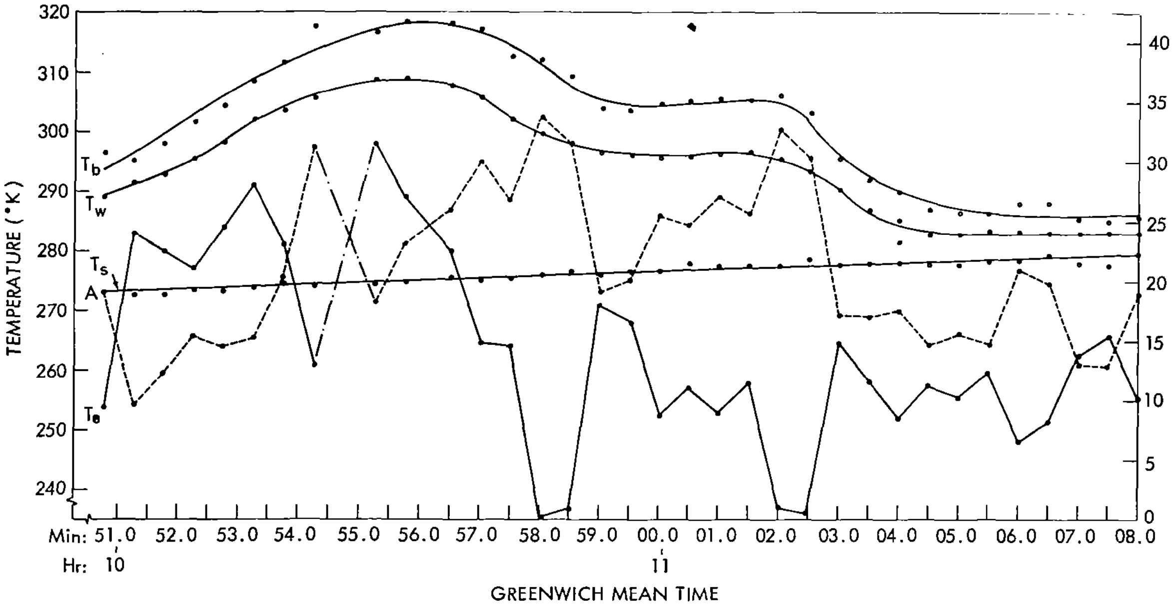

Figure 32—Reduced channel 6 data for orbit 43, Tiros III, July 15, 1961. The equilibrium detector temperatures (T_b, T_w), radiometer housing temperature (T_s), apparent earth blackbody temperature (T_e), and albedo (A) are shown as a function of time. T_e and A have been calculated from the individual points of T_b, T_w, and T_s.

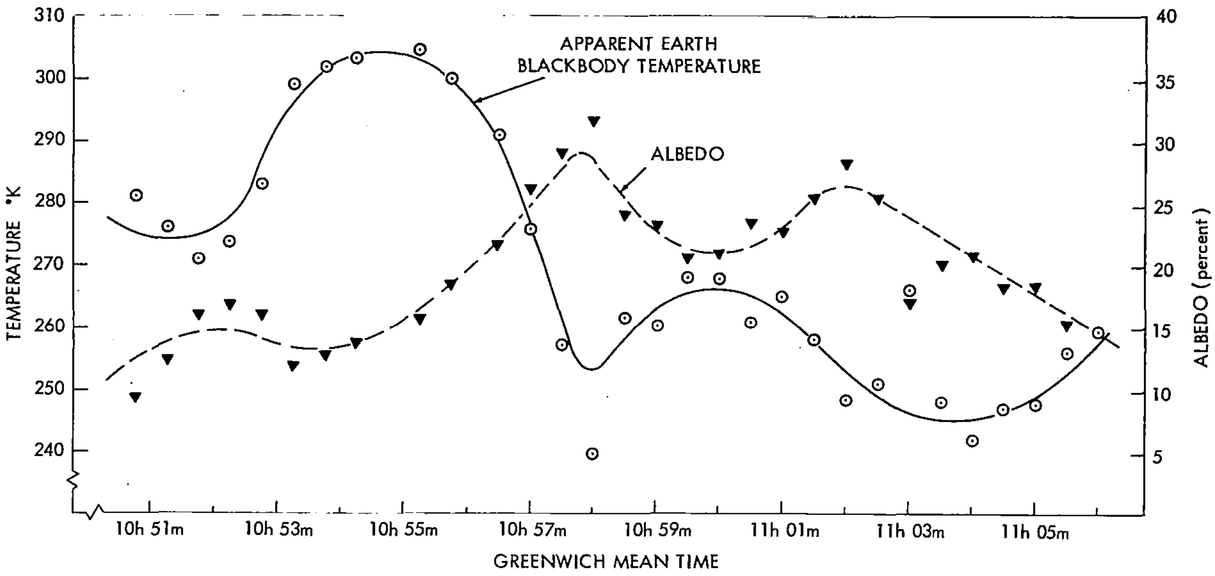

Figure 33—Smoothed results of T_e and A. T_e and A have been calculated from the curves of T_b, T_w, and T_s shown in Figure 32.

$$dT_e = \frac{1}{4T_e^3}\left(\frac{\partial T_e^4}{\partial k_{1b}}\,dk_{1b} + \frac{\partial T_e^4}{\partial k_{2b}}\,dk_{2b} + \cdots + \frac{\partial T_e^4}{\partial T_s}\,dT_s + \cdots\right) . \tag{16}$$

The evaluation of the total differentials of T_e and A was made for several different cases and the results are listed in Table 3. Mathematically, the large magnitude of the coefficients in the differentials is the reason that the small changes in detector temperatures are magnified into the resultant large changes in A and T_e. Physically, the large magnitudes of the coefficients are due to the values of the optical characteristics of the radiometer. If the k's were to meet design specifications, the magnitudes of the coefficients in the differentials would decrease and thus would tend to decrease the large fluctuations of T_e and A. Any remaining unreasonable fluctuations of T_e and A would then be inherent in the nature of the physical process.

The probable errors for A and T_e were calculated from

$$\left[\text{p.e.}(A)\right]^2 = \left(\frac{\partial A}{\partial k_{1b}}\right)^2 \left[\text{p.e.}\left(k_{1b}\right)\right]^2 + \cdots , \tag{17}$$

$$\left[\text{p.e.}\left(T_e\right)\right]^2 = \left(\frac{1}{4T_e^3}\frac{\partial T_e^4}{\partial k_{1b}}\right)^2 \left[\text{p.e.}\left(k_{1b}\right)\right]^2 + \cdots , \tag{18}$$

and are also included for the cases in Table 3. The probable errors for the various parameters in Equations 17 and 18 were assumed to be

$$\left.\begin{array}{l} \text{p.e.}\left(k_{1b}\right) \\ \text{p.e.}\left(k_{2b}\right) \\ \text{p.e.}\left(k_{1w}\right) \\ \text{p.e.}\left(k_{2w}\right) \end{array}\right\} = \pm\,0.02 ,$$

Table 3

Total Differentials and Probable Errors for the Albedo and Earth Temperature, Tiros III.

Case	Temperatures (°K)			Total Differentials for Albedo and Earth Temperature	Albedo (percent)	Earth Temperature (°K)	Probable Error (percent or °K)
	T_b	T_w	T_s				
I	285	280	273	$dA = -120\,dk_{1b} + 180\,dk_{2w} + 120\,dk_{1w} - 150\,dk_{2b} + (580\times 10^{-12})\,dk_{3w} - (490\times 10^{-12})\,dk_{3b} - 2.8\,dT_w + 2.5\,dT_b + 0.28\,dT_s$	13	-	±8
II	300	290	273	$dA = -100\,dk_{1b} + 180\,dk_{2w} + 100\,dk_{1w} - 150\,dk_{2b} + (1100\times 10^{-12})\,dk_{3w} - (860\times 10^{-12})\,dk_{3b} - 3.1\,dT_w + 3.0\,dT_b + 0.28\,dT_s$	24	-	±10
III	315	300	273	$dA = -69\,dk_{1b} + 180\,dk_{2w} + 58\,dk_{1w} - 150\,dk_{2b} + (1740\times 10^{-12})\,dk_{3w} - (1480\times 10^{-12})\,dk_{3b} - 3.5\,dT_w + 3.4\,dT_b + 0.28\,dT_s$	39	-	±14
IV	318	309	275	$dT_e = 455\,dk_{1b} + 319\,dk_{2b} + (0.16\times 10^{-8})\,dk_{3b} - 686\,dk_{1w} - 473\,dk_{2w} - (0.21\times 10^{-8})\,dk_{3w} - 7.1\,dT_b + 9.8\,dT_w - 1.2\,dT_s$	-	302	±24

$$\text{p.e.}\left(k_{3b}\right) = \pm 63 \times 10^{8}\ \frac{{}^{\circ}\text{K}^4\ \text{cm}^2}{\text{watt}}\ (\pm 5.2\ \text{percent})\ ,$$

$$\text{p.e.}\left(k_{3w}\right) = \pm 48 \times 10^{8}\ \frac{{}^{\circ}\text{K}^4\ \text{cm}^2}{\text{watt}}\ (\pm 5.9\ \text{percent})\ ,$$

$$\left.\begin{array}{l}\text{p.e.}\left(T_b\right) \\ \text{p.e.}\left(T_w\right)\end{array}\right\} = \pm 1^{\circ}\text{K}$$

$$\text{p.e.}\left(T_s\right) = \pm 0.5^{\circ}\text{K}$$

In Table 3 the probable error in the albedo can be seen to increase from ±8 to ±14 percent from case I to III with increasing $(T_b - T_w)$. For case I the contribution of any one parameter to the resultant probable error in A is equal to the contribution of any other parameter. As the $(T_b - T_w)$ interval increases, the error contributions from k_{3b} and k_{3w} become the dominant factor in the determination of the error in A. Only one case was evaluated for the probable error in T_e, which was ±24°K. As the probable error for T_e depends inversely on T_e^3, the ±24°K is a minimum error since T_e was equal to 302°K for case IV.

The resultant probable errors for T_e and A can be reduced by: (1) decreasing the magnitude of the coefficients in the expressions for the probable error (for example $\partial A/\partial k_{1b}$); or (2) reducing the probable errors of the individual parameters for example, $\left[p.e.\left(k_{1b}\right)\right]$ which are introduced by errors in data processing (errors in temperature) or calibration (errors in k's). The magnitude of the coefficients can be decreased as discussed in the previous paragraph. The errors in data processing ultimately appear in the values of T_s, T_b, and T_w and it is felt that these errors have been minimized. The errors in calibration appear in the various k constants and the reduction of these errors involves refinement of the calibration techniques. This refinement should be centered around improvement of the values for the reflected solar radiation coefficients. Specific areas in the reflected solar radiation calibration that can be improved are: solar simulator source, spectral calibration, control of intensity variation, the diffusely reflecting surface (uniformly white), and thermopile measurements. With implementation of improved procedures, it is reasonable to expect that the percentage errors for the k_3's should be reduced to the order of ±2 percent. Then, for case III the probable error in albedo would be reduced from ±14 to ±8 percent and the contribution of the individual parameters to the resultant probable error would be equal. For case I the probable error in albedo would be reduced from ±8 to ±7 percent, and for case IV, the probable error in T_e would be reduced from ±24°K to ±21°K. To further reduce the probable errors in A and T_e an overall improvement in spectral response and a reduction in conductive coupling are needed. Therefore, it is felt that the percentage errors of ±7 percent, and ±21°K in A and T_e, obtained using the improved k_3 constants, are optimum values within the state of the art limitations.

DATA COVERAGE LIMITATIONS

The value of the low resolution radiometer in measuring the heat balance of the earth is limited because of the data acquisition limitations of Tiros. Since the satellite is space oriented it is launched so that the favorable picture taking time (minimum nadir angle) occurs at local noon. Through magnetic attitude control, this relationship is maintained as nearly as possible. The optical axes of the Tiros camera and the low resolution radiometer are coincident, the low resolution radiometer field of view approximating half the angular field of view of the cameras. Therefore, in general, the low resolution radiometer data are centered, in time, within 2 hr of local noon. Initial launch conditions limit the latitudinal data coverage to the range of 48° North to 48° South. A latitudinal and longitudinal limitation is also imposed on the data coverage by precession of the satellite orbital plane and location of the interrogation stations.

The limitations imposed on low resolution radiometer data acquisition by spin stabilization, initial launch conditions, precession, and the location of interrogation stations reduce the potential of the system in obtaining short and long range planetary heat balance. Finding the value of short range heat balance, which would include investigation of diurnal effects, cannot be accomplished because the data are centered within 2 hr of local noon, and on a latitudinal and longitudinal basis only a small number of data points are available (Reference 10). The long range heat balance cannot be obtained, except as a longitudinal effect, because of insufficient earth coverage in the polar regions. Statistically, even for a long range longitudinal heat balance the number of data points available is not considered to be sufficient.

POST-LAUNCH OBSERVATIONS

The black detector network of the Tiros II and IV low resolution radiometers failed to respond to incident radiation at orbits 1373 and 1150, respectively. Radiation data were recorded for Tiros III for 2975 orbits and during this period no low resolution radiometer failures were observed.

In order to explain the analog pattern produced by the black detector network, after its failure in Tiros II and IV, it was necessary that the detector leg of the resistance network contain an open circuit. The detector leg consists of the black detector and a sensistor. The black detector is considered to be more susceptible to failure; its shape and composition allow warping and flaking of the detector element. A reasonable explanation for the failure is that thermal stress, due to expansion and contraction of the bolometer element, caused an open circuit in the detector leg. During the early stages of failure, the open circuit occurred when the thermistor element expanded because of the heating by absorption of terrestrial and reflected solar radiation. As the viewing area returned to outer space the thermistor contracted and the circuit again closed to normal. Shortly after this initial phase, the open circuit became permanent because of repeated expansion and contraction of the detector element, and the network resistance then consisted of the temperature sensitor and the fixed resistance in series.

SUMMARY OF THE TIROS LOW RESOLUTION RADIOMETER PROGRAM

Certain deficiencies of the radiometer became evident from the laboratory calibration data. Perhaps the most important was the excessive thermal coupling between the radiometer detectors and the satellite. The white detector did not adequately reflect the solar spectrum nor did it adequately absorb the terrestrial infrared emission. The cone reflectance was considered to be too low in value, thereby decreasing the optical efficiency. These two factors contribute to the excess thermal coupling with the satellite.

The above deficiencies manifested themselves in the reduced data by contributing to the large errors in the resultant values of T_e and A as shown in the orbit 43 data. Some of the resultant error is inherent in the physical nature of the process, since the solution of the heat transfer equations for T_e and A involves temperatures to the fourth power and differences of large numbers. Additional sources of error in T_e and A are errors in data processing and calibration.

A considerable amount of radiation data has been obtained from the Tiros III and IV low resolution radiometers. To date, only a few orbits of these data have been studied extensively because the automatic data reduction system is not yet operational. Because of large uncertainties, the absolute values of T_e and A have limited application in studies utilizing the radiation data. However, the relative measurements of T_e and A should still provide useful information for the areas on the earth where data are available.

IMPROVEMENT EFFORTS

Further improvement of a low resolution radiometer was attempted for the second generation weather satellite, Nimbus. The objectives were to improve the radiometer performance by:

1. Reducing the excessive thermal coupling between the radiometer detectors and the satellite.
2. Improving the reflection coatings on the reflecting cones so that they would adequately reflect all radiation onto the detectors.
3. Improving the infrared absorptance and solar reflectance of the white detector. Also, since Nimbus will be earth oriented, the deterioration of the white coating from ultraviolet radiation exposure becomes more important than it was in the Tiros radiometer.

The initial effort was centered on reducing the coupling effects. The approach to the investigation of this problem was to employ a different method of mounting the detector at the terminal base of the cone, use different schemes for the electrical leads from the detector, and try to minimize the applied bias power. These investigations indicated that the degree of coupling could not be significantly improved over that attained with the Tiros radiometer.

A white coating (Naval Research Laboratory Type II) was found which did not show much deterioration from ultraviolet exposure and which had a solar-weighted reflectance of 75-80 percent. However, this paint was somewhat deficient in absorption in the infrared. The cone reflectance was improved by a better aluminizing technique.

With the present state-of-the-art limitations, further improvements of the deficiencies could not be made, since the radiometer was to be a low cost experiment. Therefore, development of a low resolution radiometer for Nimbus was discontinued.

CONCLUSION

The evaluation of the calibration data indicated that a strong thermal coupling existed between the radiometer detectors and the satellite and that the white detector coating and the cone optics were inadequate in spectral response. Improvement of these deficiencies would aid in reducing the probable errors of A and T_e, which were found to be approximately ±8 to ±14 percent and ±24°K, respectively. With the present experiment, it is expected that improvement in the reflected solar radiation calibration could reduce the probable error in A to approximately ±7 percent and in T_e to approximately ±21°K.

For the Tiros low resolution radiometer, limitations on data coverage reduce the value of the data for heat balance studies. However, the relative measurements of T_e and A still should provide useful information for the areas on the earth where data are available.

Efforts to improve the performance of the low resolution radiometer were only partially successful because of limitations of the state-of-the-art. Development was discontinued because of the disproportionate cost in achieving an instrument which was to be of low cost.

ACKNOWLEDGMENTS

The authors wish to thank Dr. W. Nordberg and Mr. W. R. Bandeen for their critical review of this work. The assistance of Mr. R. Carter in performing the calibrations is also acknowledged.

(Manuscript received January 9, 1964)

REFERENCES

1. Stroud, W. G., "Initial Results of the Tiros I Meteorological Satellite," *J. Geophys. Res.* 65(5):1643-1644, May 1960.
2. Sternberg, S., and Stroud, W. G., "Tiros I—Meteorological Satellite," *Astronautics* 5(6):32-34, 84-86, June 1960.
3. Bandeen, W. R., Hanel, R. A., Licht, J., Stampfl, R. A., and Stroud, W. G., "Infrared and Reflected Solar Radiation Measurements from the Tiros II Meteorological Satellite," NASA Technical Note D-1096, November 1961; also *J. Geophys. Res.* 66(10):3169-3185, October 1961.
4. Astheimer, R. W., De Waard, R., and Jackson, E. A., "Infrared Radiometric Instruments on Tiros II," *J. Opt. Soc. Amer.* 51(12):1386-1393, December 1961.
5. Hanel, R. A., "A Low-Resolution Unchopped Radiometer for Satellites," NASA Technical Note D-485, 1961; also *Amer. Rocket Soc. J.* 31(2):246-250, February 1961.
6. Johnson, F. S., "The Solar Constant," *J. Meteorol.* 11(6):431-439, December 1954.
7. Reid, C. D., and McAlister, E. D., "Measurement of Special Emissivity from 2μ to 15μ," *J. Opt. Soc. Amer.* 49(1):78-82, January 1959.
8. Davis, J. F., Hanel, R. A., Stampfl, R. A., Strange, M. G., and Townsend, M. R., "Telemetering Infrared Data from the Tiros Meteorological Satellites," NASA Technical Note D-1293, August 1962.
9. Nordberg, W., Bandeen, W. R., Conrath, B. J., Kunde, V., and Persano, I., "Preliminary Results of Radiation Measurements from the Tiros III Meteorological Satellite," *J. Atmos. Sci.* 19(1):20-30, January 1962.
10. Bignell, K. J., "Heat-Balance Measurements from an Earth Satellite—an Analysis of some Possibilities," *Quart. J. Roy. Meteorol. Soc.* 87:231-244, April 1961.

NASA-Langley, 1964 G-564